Homophilic CD44 Interactions Mediate Tumor Cell Aggregation and Polyclonal Metastasis in Patient-Derived Breast Cancer Models

Xia Liu[1], Rokana Taftaf[1], Madoka Kawaguchi[1], Ya-Fang Chang[2], Wenjing Chen[1], David Entenberg[3], Youbin Zhang[4], Lorenzo Gerratana[4,5], Simo Huang[6], Dhwani B. Patel[1], Elizabeth Tsui[1], Valery Adorno-Cruz[1,7], Steven M. Chirieleison[6], Yue Cao[8], Allison S. Harney[3], Shivani Patel[6], Antonia Patsialou[3], Yang Shen[8], Stefanie Avril[6], Hannah L. Gilmore[6], Justin D. Lathia[9,10], Derek W. Abbott[6], Massimo Cristofanilli[4,11], John S. Condeelis[3], and Huiping Liu[1,4,6,11]

ABSTRACT

Circulating tumor cells (CTC) seed cancer metastases; however, the underlying cellular and molecular mechanisms remain unclear. CTC clusters were less frequently detected but more metastatic than single CTCs of patients with triple-negative breast cancer and representative patient-derived xenograft models. Using intravital multiphoton microscopic imaging, we found that clustered tumor cells in migration and circulation resulted from aggregation of individual tumor cells rather than collective migration and cohesive shedding. Aggregated tumor cells exhibited enriched expression of the breast cancer stem cell marker CD44 and promoted tumorigenesis and polyclonal metastasis. Depletion of CD44 effectively prevented tumor cell aggregation and decreased PAK2 levels. The intercellular CD44–CD44 homophilic interactions directed multicellular aggregation, requiring its N-terminal domain, and initiated CD44–PAK2 interactions for further activation of FAK signaling. Our studies highlight that $CD44^+$ CTC clusters, whose presence is correlated with a poor prognosis of patients with breast cancer, can serve as novel therapeutic targets of polyclonal metastasis.

SIGNIFICANCE: CTCs not only serve as important biomarkers for liquid biopsies, but also mediate devastating metastases. CD44 homophilic interactions and subsequent CD44–PAK2 interactions mediate tumor cluster aggregation. This will lead to innovative biomarker applications to predict prognosis, facilitate development of new targeting strategies to block polyclonal metastasis, and improve clinical outcomes.

See related commentary by Rodrigues and Vanharanta, p. 22.

Downloaded from http://aacrjournals.org/cancerdiscovery/article-pdf/9/1/96/1847835/96.pdf by guest on 27 August 2022

[1]Department of Pharmacology, Feinberg School of Medicine, Northwestern University, Chicago, Illinois. [2]The Ben May Department for Cancer Research, The University of Chicago, Chicago, Illinois. [3]Deparment of Anatomy and Structural Biology, Gruss Lipper Biophotonics Center, Integrated Imaging Program, Albert Einstein College of Medicine, Bronx, New York. [4]Department of Medicine, Hematology/Oncology Division, Feinberg School of Medicine, Northwestern University, Chicago, Illinois. [5]Department of Medicine (DAME), University of Udine, Udine, Italy. [6]Deparment of Pathology, School of Medicine, Case Western Reserve University, Cleveland, Ohio. [7]Department of Pharmacology, School of Medicine, Case Western Reserve University, Cleveland, Ohio. [8]Department of Electrical and Computer Engineering, TEES-AgriLife Center for Bioinformatics and Genomic Systems Engineering, Texas A&M University, College Station, Texas. [9]Department of Cellular and Molecular Medicine, Cleveland Clinic Lerner Research Institute, Cleveland, Ohio. [10]The Case Comprehensive Cancer Center, Cleveland, Ohio. [11]Robert H. Lurie Comprehensive Cancer Center, Feinberg School of Medicine, Northwestern University, Chicago, Illinois.

Note: Supplementary data for this article are available at Cancer Discovery Online (http://cancerdiscovery.aacrjournals.org/).

Corresponding Authors: Huiping Liu, Northwestern University, 303 East Superior Street, Lurie 5-119, Chicago, IL 60611. Phone: 312-503-5248; Fax: 312-503-0189; E-mail: huiping.liu@northwestern.edu; John S. Condeelis, Gruss Lipper Biophotonics Center, Integrated Imaging Program, Albert Einstein College of Medicine, Bronx, NY 10461. E-mail: john.condeelis@einstein.yu.edu; and Xia Liu, Northwestern University, Feinberg School of Medicine, Department of Pharmacology, Chicago, IL 60611. E-mail: xia.liu@northwestern.edu

doi: 10.1158/2159-8290.CD-18-0065

©2018 American Association for Cancer Research.

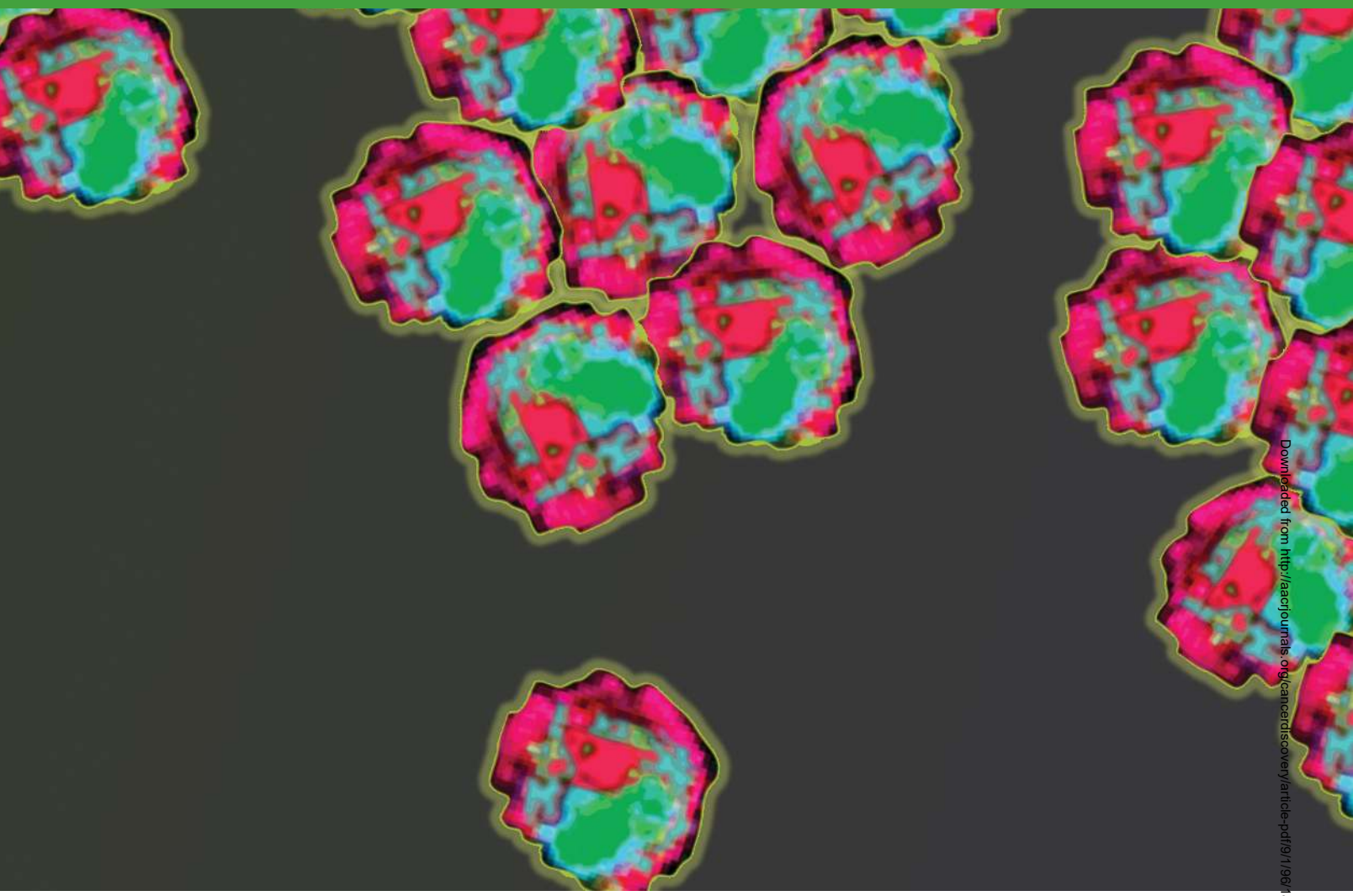

Downloaded from http://aacrjournals.org/cancerdiscovery/article-pdf/9/1/96/1847835/96.pdf by guest on 27 August 2022

INTRODUCTION

Circulating tumor cells (CTC) spread from established tumors, circulate within the peripheral vasculature, and lead to the development of distant metastases that account for 90% of solid tumor–related mortality. Although many tumor cells may shed from a primary tumor, only an extremely small proportion of the CTCs can form secondary tumors (1–3). Both our studies and others' have shown that the clustered CTCs detectable in the peripheral blood of patients with breast cancer are associated with a worse prognosis than single CTCs (4, 5). However, there is a lack of mechanistic understanding about which cellular and molecular properties enable tumor cluster formation and colonization and which targets may be used to block this metastatic pathway.

Increasing evidence has demonstrated that cancer stem cell (CSC) properties contribute to tumor initiation, recurrence, and therapy resistance (6–17). CD44 is a well-known surface marker of CSCs in breast tumors (9, 18, 19) and other tumors (20–22). However, the functional contributions of CSCs and CD44 to CTC cluster formation and polyclonal metastasis are yet to be elucidated.

We decided to dissect this mechanism of cancer metastasis by establishing and utilizing breast cancer patient–derived xenograft (PDX) models. We previously established five breast cancer PDX models (TN1–4 and E1; ref. 17) and recently created two more orthotopic breast tumor PDXs (TN5–6), six of which (TN1–6) were triple negative (TN) for estrogen receptor, progesterone receptor, and HER2, that developed spontaneous lung micrometastases in NOD/SCID or NSG mice. Two PDXs (TN1 and TN2) showed basal-like subtype gene-expression profiles based on cDNA microarray analyses (23). Human breast cancer MDA-MB-231 cells and mouse PyMT transgenic tumor models (24, 25) have also been supplemented for the intravital imaging analyses as well as the cellular and molecular understanding of cluster formation.

Our studies here set out to determine how tumor cell clusters are generated *in vivo*, whether the CSC marker CD44 is enriched within CTC clusters and required for tumor cell cluster formation, and what downstream targets of CD44 are essential players to promote tumor cluster–mediated metastasis. Using mass spectrometry analyses, we have identified p21 protein (CDC42/RAC)–activated kinase 2 (PAK2) as a new CD44 target. PAK2 is a member of the evolutionarily conserved group I PAK family of serine/threonine protein

kinases, along with PAK1/3 (26). The role of PAK2 in breast tumor cell cluster formation has been elucidated below.

RESULTS

CTC Cluster Detection in Humans and PDXs with Metastatic Breast Cancer

CTC detection in humans is typically accomplished with blood analysis platforms such as the FDA-approved CellSearch, which analyzes EPCAM-positive CTCs with additional cytokeratin (CK)-positive and CD45-negative markers (27). In mouse models of cancer, tumor cells are labeled by fluorescent proteins eGFP or tdTomato, and thus blood CTCs are detected in an unbiased manner using fluorescence microscopy of peripheral blood cells after depletion of erythrocytes. Complementary to blood CTC analyses, we also used vascular CTC detection in tissue sections by histochemical staining as well as in tumor models by intravital fluorescence imaging, thereby enhancing our cellular and molecular understanding of the CTC clusters in human breast cancer.

On the basis of tissue section availability, we first used IHC staining–based analyses of tissue sections, including staining with hematoxylin and eosin (H&E), epithelial markers CK or EPCAM, and endothelial marker CD31, to detect *in situ* CTCs within the vasculature (Fig. 1A and B; Supplementary Fig. S1A–S1D). We analyzed IHC-based vascular CTCs within tissue sections of primary tumors and distant metastases collected from seven patients with breast cancer at Case Western Reserve University (CW1–7; $n = 9$ tissue sections) and seven PDX models (TN1–6 and E1; $n = 45$ lung sections from 45 mice, respectively), among which TN5–6 were newly established (Supplementary Table S1). Clustered and single CTCs were detected within the vasculature of tissue sections, at similar frequencies (30%–40% cluster events) and with similar morphology between human TN breast cancer and PDX specimens (Fig. 1A–C; Supplementary Fig. S1A–S1D; Supplementary Table S1).

Using the CellSearch-based blood analysis, which normally detects single CTCs, we also detected CTC clusters (Fig. 1D) in a small proportion (7 of 46) of blood specimens collected from patients with metastatic breast cancer at Northwestern University (Supplementary Table S2). To determine whether the blood CTCs cluster in PDXs, we transduced four breast tumor PDXs with optical reporters, including eGFP, tdTomato, luciferase 2-eGFP (L2G), and luciferase 2-tdTomato (L2T), as previously described (17). In the L2G and L2T single-color and mixed-color implants of PDXs and MDA-MB-231 models, we observed both single-color and dual-color CTC clusters as well as polyclonal lung metastases of both eGFP$^+$ and tdTomato$^+$ tumor cells (Fig. 1E; Supplementary Fig. S2A–S2E), which is consistent with previous reports from cell lines (5) and mouse tumor models (28). CTC clusters in the blood were detected at similar frequencies (8%–10% clustered events) between patients ($n = 7$ patients, 15 blood specimens) and PDX models ($n = 4$ models, 7 blood specimens; Fig. 1F; Supplementary Table S2).

We then compared the frequencies of dual-color, polyclonal lung colonies between mixed-color implants and the separate-color implants of TN1 PDXs as shown in Supplementary Fig. S2A. In total, a high proportion (54% ± 15%; $n = 8$ mice) of lung colonies of 2 to 10 tumor cells were dual color in the images of mice bearing mixed L2G–L2T implants in both mammary fat pads (Supplementary Fig. S2C and S2D), suggesting advantageous clustering from mixed tumor cells in close proximity. In contrast, a low proportion of lung colonies (10% ± 4%; $n = 8$ mice, $P < 0.0001$) from separate-color implants exhibited dual color when the L2T- and L2G-labeled tumor cells were separately implanted into two distinct fat pads on the left and the right, respectively (self-seeding or cross-seeding was not observed; Supplementary Fig. S2C and S2D). This suggested that these distantly separated green and red tumor cells might meet in the vasculature or the lungs to form dual-color lung colonies.

Figure 1. Tumor cell clusters arise from cellular aggregation. **A,** H&E staining images of CTC clusters (orange arrows) within the vasculature of the lung metastasis (met) sections of TN breast cancer patient CW1 (left) and a TN1 PDX mouse (right). Scale bars, 10 μm. **B,** IHC staining with a TN PDX breast tumor section for cytokeratin (CK) showing clustered tumor cells within the vasculature (a lower magnification image is shown in Supplementary Fig. S1B). Scale bar, 10 μm. **C,** Frequencies of IHC-detected vascular CTC clusters (% of all CTC events) within breast tumor and distant metastasis sections of seven patients ($n = 9$ human tissues) and seven PDX models ($n = 28$ mouse tissues; listed in Supplementary Table S1). *t* test $P = 0.1115$ (NS). **D,** Human CTC clusters in the peripheral blood of patients with metastatic breast cancer, negative for CD45 and positive for pan-CK and nuclear DNA (DAPI), detected via EPCAM-based CellSearch platform. Scale bars, 10 μm. **E,** Fluorescence images of TN1 PDX tumor cell clusters within the peripheral blood and the lungs of NOD/SCID mice. Top, blood CTC cluster (tdTomato$^+$) from L2T PDX-bearing mice (blue, Hoechst). Bottom, 3-D stack image of a dual-color lung colony with one L2G (eGFP$^+$) cell and one L2T (tdTomato$^+$) cell derived from mixed-color implants as shown in Supplementary Fig. S2A. Scale bars, 10 μm. **F,** Frequencies of blood CTC clusters (% of all CTC events) isolated from seven patients with metastatic breast cancer ($n = 7$) and mice with 4 PDX models ($n = 7$ mice; Supplementary Table S2). *t* test $P = 0.533$ (NS). **G,** Intravital images of TN1 PDX breast tumor cell cluster formation via cell aggregation during migration, showing individually migrating eGFP$^+$ tumor cells approaching and aggregating with other tumor cells and moving around dynamically. Arrows at 24′ and 30′ show the cumulative paths of cells 1, 2, and 3. Red, dextran$^+$ vessels; blue, second harmonic generation (collagen I fibers). Scale bar, 10 μm. See Supplementary Video S1. **H,** Intravital images of single-cell intravasation of eGFP$^+$ MDA-MB-231 tumor cells following cluster formation in a primary tumor. Stationary tumor cell 1 is joined by individually migrating cells 2 and 3 to form a cluster. Cell number 2 sequentially leaves the cluster and intravasates between the frames at 18′ and 20′. Green, tumor cells; red, vasculature. Scale bar, 10 μm. See Supplementary Video S3. **I,** Intravital images of eGFP$^+$ PyMT breast tumor cells (yellow in the red vasculature) in MacBlue Rag$^{-/-}$ mice, circulating as single cells (T1 and T5) and as groups of cells (T2, T3, and T4) in close physical proximity to each other. Tumor cells are briefly observed as they rapidly pass through the imaging field due to blood flow. Green, tumor cells (CTCs shown yellow); red, 155 kD TMR–dextran-labeled vasculature; cyan, macrophages (circulating monocytes in white in the red vasculature). Scale bar, 10 μm. Additional CTCs in Supplementary Video S4. **J,** Patient-derived CTC line BRX50 cells form clusters within 1 to 2 hours of suspension culture. Scale bar, 50 μm. **K,** Cluster formation within the lung vasculature imaged *ex vivo* at 2 hours after tail-vein infusion of eGFP$^+$ (green) and tdTomato$^+$ (red) MDA-MB-231 cells at 1:1 ratio, either mixed coinfusion (0 minutes apart), or separate infusions of tdTomato$^+$ cells first and then eGFP$^+$ cells lagged at 5 minutes, 10 minutes, and 2 hours. *Ex vivo* lung fluorescence images were taken 2 hours after infusion of eGFP$^+$ cells. Scale bars, 50 μm. **L,** Quantitative proportions of single-color and mixed-color clusters (lung colonies) from the four groups in **K**. The experiments were repeated three times ($n = 3$) with counts of at least five images per mouse. *t* test ***, $P < 0.001$.

Downloaded from http://aacrjournals.org/cancerdiscovery/article-pdf/9/1/96/1847835/96.pdf by guest on 27 August 2022

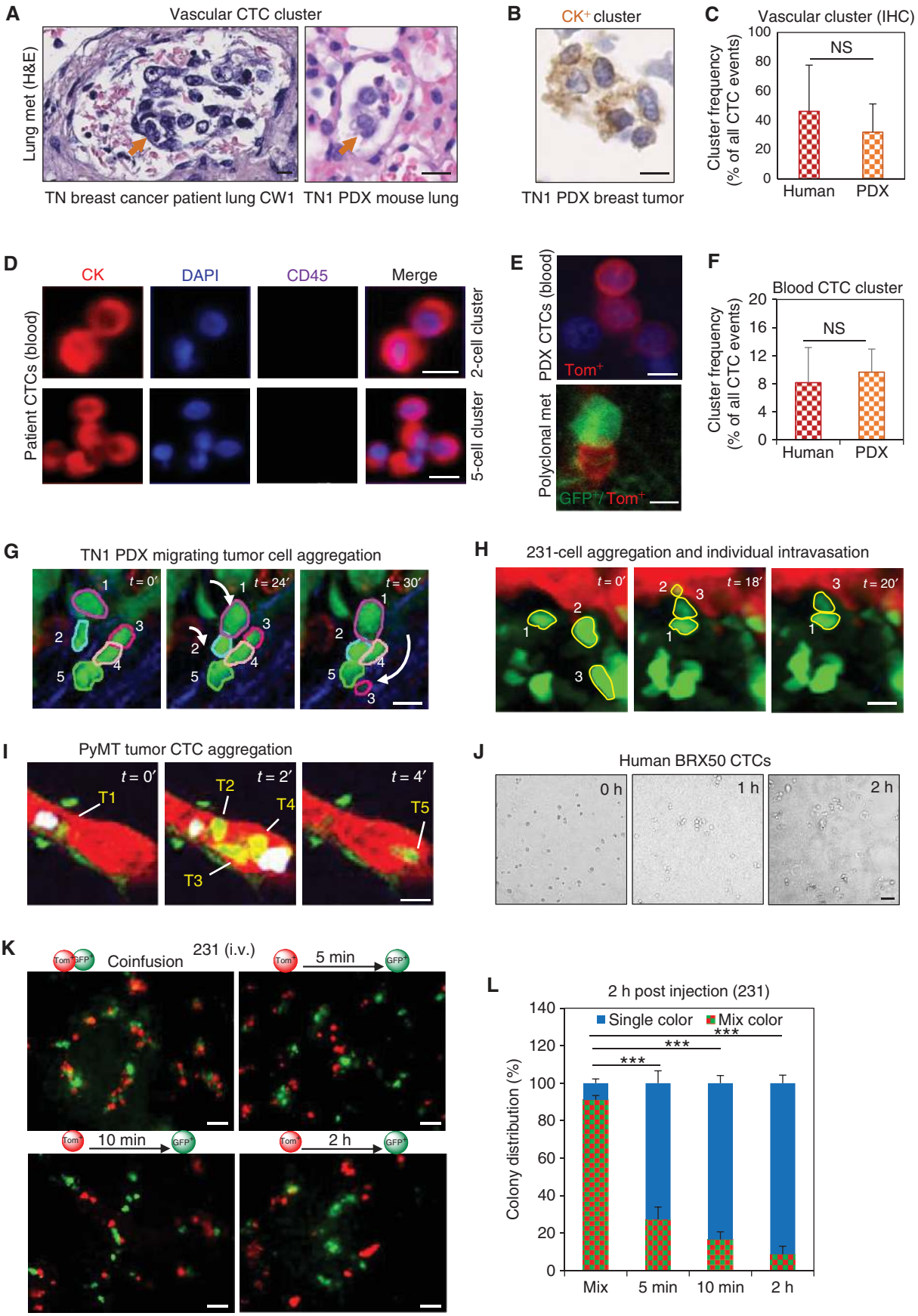

Downloaded from http://aacrjournals.org/cancerdiscovery/article-pdf/9/1/96/1847835/96.pdf by guest on 27 August 2022

Breast Tumor Cell Clusters Arise from Aggregation of Individual Tumor Cells

In order to explore the cellular mechanisms of polyclonal cluster formation, we used intravital multiphoton microscopic imaging of the TN1 PDX breast tumors, human MDA-MD-231 cell–derived tumor models, and mouse PyMT transgenic tumor models as described (24, 25). We observed that individual migrating tumor cells aggregated into clusters near the vasculature in a dynamic touch-and-go manner (Fig. 1G; Supplementary Fig. S3A; Supplementary Videos S1 and S2). Some individual tumor cells detached from the cluster and subsequently entered singly into the adjacent blood vessel (Fig. 1H; Supplementary Video S3). Notably, certain CTCs remained in close proximity with each other within the tumor vasculature even during rapid blood flow, shown by snapshots and videos of intravital imaging (Fig. 1I; Supplementary Video S4).

Using the TN PDXs that display individual cell migration patterns (17, 24) under intravital imaging (29, 30), we collected invasive tumor cells *in vivo* from these models to examine the cellular patterns upon invasion into chemoattractant-containing Matrigel. We found that around 20% of all counted invasion events occurred as multicellular aggregates (Supplementary Fig. S3B). We also observed that individual CTCs derived from breast cancer patient BRX-50 (31) at Massachusetts General Hospital (provided by Dr. Daniel Haber) aggregated into multicellular clusters in suspension culture within 1 to 2 hours (Fig. 1J), suggesting individual cell aggregation as a possible mechanism of CTC cluster formation.

We then sought to determine whether the frequency of polyclonal CTC aggregation and lung colonization is dependent on the timing of multiple individual tumor cells entering into blood vessels and homing to the lungs. Upon coinfusion (0 minutes apart) of both eGFP$^+$ and tdTomato$^+$ single breast tumor cells (MDA-MB-231 cells) via the tail vein, most of the eGFP$^+$ and tdTomato$^+$ tumor cells cohomed, resulting in a high ratio of dual-color aggregates of up to 5 cells (92%) within 2 hours in the lungs (Fig. 1K and L). In contrast, sequential infusion of these tumor cells with separations of 5 minutes, 10 minutes, and 2 hours led to gradually decreased ratios of dual-color aggregates (foci) in the lungs (27%, 16%, and 10%, respectively) when imaged 2 hours after the final injection (Fig. 1K and L). These studies demonstrate that given a close temporal and spatial proximity of intravasation, individual CTCs are capable of aggregating into clusters in the circulation or lung vasculature. This might contribute to the higher percentage of dual-color lung colonies in mixed-color implants than in separate-color implants as shown in Supplementary Fig. S2C and S2D.

Aggregated Tumor Cells Promote Tumorigenesis and Metastasis

Following this finding, we hypothesized that CSCs contribute to tumor cell aggregation and sought to determine whether tumor cell aggregates have better CSC-related properties (cancer stemness) and what molecular mechanisms might underlie this aggregation phenotype. To facilitate a mechanistic understanding, we optimized an *ex vivo* aggregation assay with dissociated PDX tumor cells and monitored real-time cell aggregation using time-lapse IncuCyte imaging (Supplementary Fig. S4A and S4B; Supplementary Video S5). After seeding, individual primary tumor cells (tdTomato$^+$ or eGFP$^+$) started to aggregate within 2 to 3 hours and continued to form bigger clusters overnight with minimal cell divisions, monitored under the time-lapse IncuCyte microscopy imaging (automatically scanned to the same fields every 2 hours). Minimal cell death was observed within the first 12 hours but became more significant only in single cells after 24 hours, demonstrating the survival advantage of clustered cells (Supplementary Fig. S4B).

We then set out to determine the CSC-related properties (32, 33) of aggregated tumor cell clusters from TN PDXs, such as orthotopic tumorigenesis (gold-standard CSC assay), mammosphere formation, and lung metastasis. We orthotopically implanted single and clustered PDX cells (TN1 and TN2) in equivalent cell numbers separately into the fourth left and right mammary fat pads of each NOD/SCID or NSG mouse. Compared with the respective single tumor cells, the clusters derived from both TN1 and TN2 PDXs were more capable of initiating tumor growth, measured by bioluminescence signal intensity over 2 to 4 weeks (Fig. 2A–D). The clustered tumor cells from the PDXs formed mammospheres at a 3.5-fold higher efficiency compared with their single-cell counterparts in serum-free mammary epithelial stem cell media *ex vivo* (Fig. 2E and F). We also observed that dissociated MDA-MB-231 tumor cells formed aggregates in suspension culture as early as within 1 hour and continued to expand up to 96 hours, while protein levels of the pluripotency-related OCT 3/4 increased over this time frame (Supplementary Fig. S5A and S5B).

We continued to compare the stemness-requiring metastatic potential between single and clustered tumor cells

Downloaded from http://aacrjournals.org/cancerdiscovery/article-pdf/9/1/96/1847835/96.pdf by guest on 27 August 2022

Figure 2. Tumor cell clusters with increased tumorigenesis, metastasis, and CD44 expression. **A,** Representative bioluminescence images of single cells (S) and clusters (C) of TN1 PDX tumor cells in parallel during tumorigenic monitoring upon orthotopic implantation (1,000 cells per mammary fat pad), on days 0 (D0) and 18 (D18). **B,** Quantitative bioluminescence signals (total flux, p/s; left) and fold change (right) of tumorigenesis mediated by TN1 tumor cells in singles and clusters during the 18-day monitoring in **A** ($n = 5$). *t* test **, $P < 0.01$. **C,** Representative bioluminescence images of single cells (S) and clusters (C) of TN2 PDX tumor cells in parallel during tumorigenic monitoring upon orthotopic implantation (5,000 cells per mammary fat pad), on days 0 (D0) and 24 (D24). **D,** Quantitative bioluminescence signals (total flux, p/s; left) and fold change (right) of tumorigenesis mediated by TN2 tumor cells in singles and clusters during the 24-day monitoring in **C** ($n = 8$). *t* test *, $P < 0.05$; **, $P < 0.01$; ***, $P < 0.001$. **E,** Images of mammospheres derived from single and clustered tumor cells of TN2 PDXs. Scale bars, 50 μm. **F,** Quantitated bar graph of mammospheres derived from single cells and clusters. $N = 6$ biological replicates. *t* test ***, $P = 0.0008$. **G,** Bioluminescence imaging (BLI) images of lung colonization mediated by single cells and clusters of L2T-labeled TN1 PDX cells (5×10^5) at day 0 (D0) and weeks 1, 2, and 8 (Wk1, 2, and 8) after tail-vein infusion. **H,** Quantitated BLI signal (total flux, p/s) of the TN1 single cell– and cluster-mediated lung metastases described in **G** ($n = 5$). *t* test *, $P = 0.012$; ***, $P = 0.00012$. **I,** CD44 (brown) and CD31 (pink) IHC staining of the TN1 PDX-bearing mouse lung sections (slide 228) showing a CD44$^+$ CTC cluster within CD31$^+$ vasculature. Scale bar, 25 μm. **J,** Proportion of CD44$^+$ CTCs in the events of single and cluster CTCs counted within the *in situ* vasculature of human breast tumors ($n = 5$) and metastases ($n = 3$), and PDX lung metastases ($n = 3$; Supplementary Table S3). *t* test ****, $P < 0.0001$.

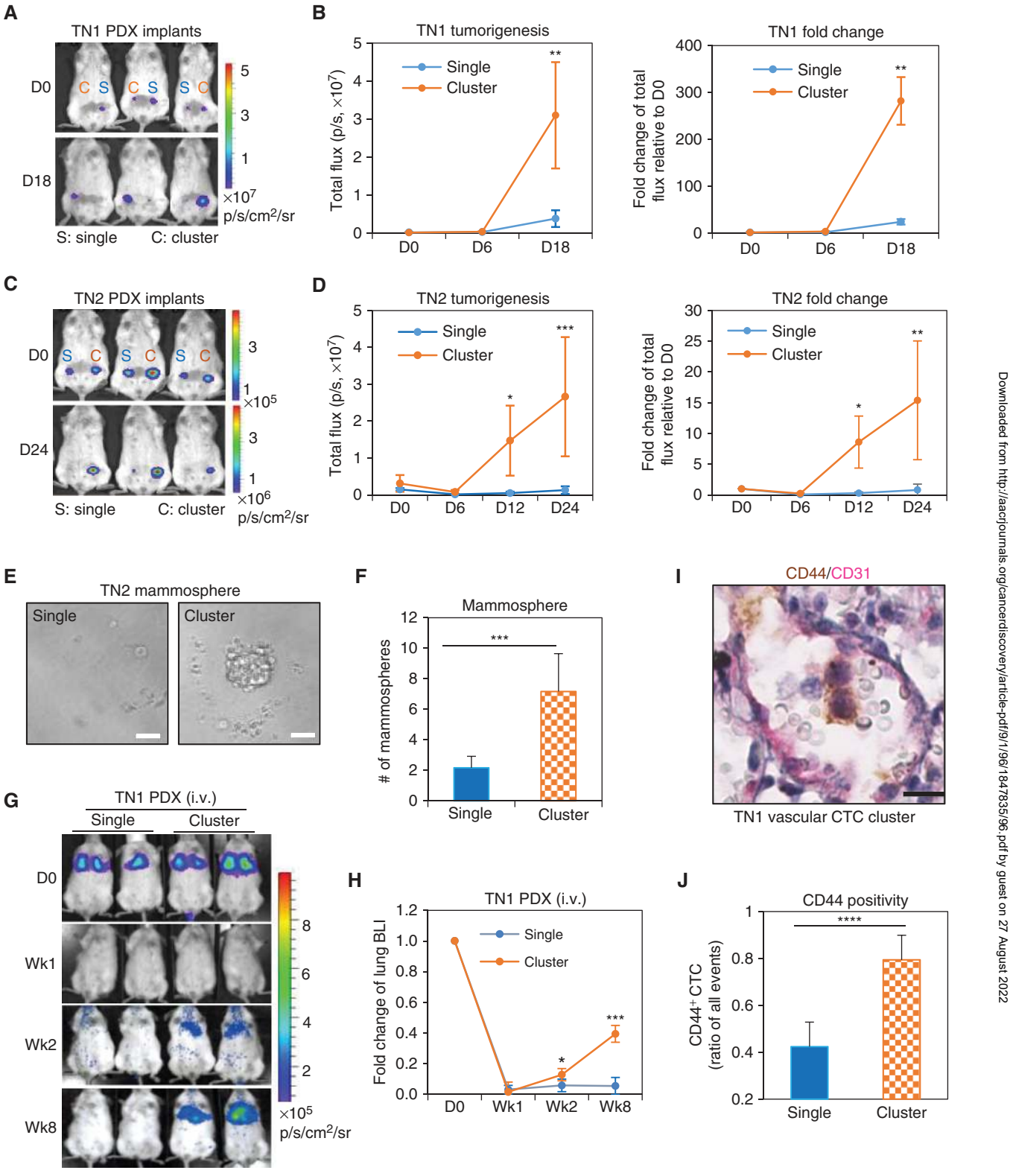

Downloaded from http://aacrjournals.org/cancerdiscovery/article-pdf/9/1/96/1847835/96.pdf by guest on 27 August 2022

derived from TN PDXs by directly injecting tumor cells into the tail vein and examining the lungs. Unlike single MDA-MB-231 breast tumor cells, which aggregated with high efficiency within 2 hours of tail-vein infusion (Fig. 1K), TN PDX-derived L2T$^+$ single tumor cells had a low efficiency in forming aggregated clusters of ≥3 to 5 cells (Supplementary Fig. S5C and S5D). Meanwhile, the injected clusters had a short-term survival advantage in the lungs at 24 hours (Supplementary Fig. S5C and S5D). Although the bioluminescence signals of clustered and single tumor cells both dropped to about 2% within 1 week, only the aggregated tumor cells recovered and regained metastatic growth within 2 to 8 weeks (Fig. 2G and H), demonstrating that the clusters have CSC properties that increase their tumorigenic and metastatic potential.

We then questioned whether markers of CSCs were detectable in clustered CTCs. CD44 and ALDH have been among the most commonly used markers of CSCs in breast tumors and many epithelial tumors (9, 18–22, 34). Although the ALDH signal was undetectable in TN PDXs (data not shown), we detected CD44 expression in the CTC clusters *in situ* within the endothelial CD31$^+$ vasculatures of PDX tumor specimens and human tissues (Fig. 2I; Supplementary Fig. S5E). Out of 384 total counted CTC events (n = 10 specimens), CD44 was notably enriched in vascular CTC clusters (100% in the PDX models, 72%–90% in human sections) as opposed to single CTCs (average 42%, $P = 2.16 \times 10^{-05}$; Fig. 2J; Supplementary Table S3).

CD44 Is Required for Tumor Cell Aggregation and Lung Colonization

To determine the functional importance of CD44 in tumor cell aggregation and subsequent lung colonization, we evaluated the effects of modulated CD44 levels on breast tumor cell aggregation, spontaneous lung metastasis upon orthotopic implantation, and lung colonization via tail-vein injection.

We first sorted CD44$^+$ and CD44$^-$ tumor cells from L2G-labeled TN PDXs for aggregation assays *ex vivo* and observed that CD44$^+$ tumor cells formed clusters not only of a bigger size but also in a larger quantity than CD44$^-$ tumor cells (Supplementary Fig. S6A–S6C). To compare CD44$^+$ and CD44$^-$ cells simultaneously in a competitive cellular aggregation course, we utilized the identical TN PDXs labeled with eGFP or tdTomato (17). We first sorted CD44$^+$ and CD44$^-$ tumor cells separately from these PDXs, each tagged either green or red, for mixed-color aggregation assays. Although the double-positive mixture of eGFP$^+$CD44$^+$ and tdTomato$^+$CD44$^+$ cells formed large, dual-color aggregates together (Fig. 3A, left; Supplementary Video S6), the double-negative mixture of eGFP$^+$CD44$^-$ and tdTomato$^+$CD44$^-$ tumor cells did not form comparable aggregates in either color (Fig. 3A, middle; Supplementary Video S7). Furthermore, when eGFP$^+$CD44$^-$ tumor cells were mixed with tdTomato$^+$CD44$^+$ tumor cells, only the red CD44$^+$ tumor cells formed distinct aggregates, whereas the green CD44$^-$ cells remained as single cells after 24 hours of *ex vivo* aggregation culture in the mammary epithelial stem cell medium (Fig. 3A, right; Supplementary Video S8). There was no significant difference observed between the numbers of viable CD44$^+$ and CD44$^-$ tumor cells during the 24-hour aggregation (Fig. 3B), suggesting that the effect of CD44 on cell aggregation is prior to any effects of cell survival. However, after a culture of 48 to 72 hours, the aggregated primary tumor cells showed a survival advantage over the nonaggregated single cells (Supplementary Fig. S6D).

To examine the requirement of CD44 for tumor cell aggregation, we knocked down CD44 in L2G-labeled TN PDX tumor cells using a mixture of commercially available CD44 siRNAs. We found that PDX-derived tumor cells mainly expressed CD44 splicing variant forms (CD44v) at ~150 kD (Fig. 3C; Supplementary Fig. S6E). To determine if CD44 regulation of tumor cell aggregation is dependent on the variant isoforms, we utilized MDA-MB-231 breast tumor cells (also TN), which exclusively express CD44 standard form (CD44s) with a smaller molecular weight of ~80 kD, which can be depleted by CD44 siRNA (si*CD44*)–mediated knockdown (Fig. 3D). To complement the transient knockdown studies, we also knocked out CD44 in eGFP (L2G) or tdTomato (L2T)–labeled MDA-MB-231 cells and TN1 PDXs using CRISPR/Cas9 technology (35) and custom-designed guide RNAs (gRNA) targeting exon 2 of the *CD44* gene (see Supplementary Methods). CD44 immunoblotting verified the depletion of CD44 in three batches of pooled knockout (KO) tumor cells (Fig. 3E).

Consistent with sorted CD44$^-$ cells (Supplementary Fig. S6B and S6C), the CD44 knockdown decreased the cluster-forming capacity of PDX-derived tumor cells, with smaller cluster size and fewer cluster numbers observed per image (Fig. 3F and G). Reduction of CD44s by si*CD44* also inhibited the aggregation of MDA-MB-231 tumor cells during the first 60 minutes in suspension (Fig. 3H and I). These data suggest that the key role of CD44 in mediation of immediate tumor cell aggregation is independent of its isoforms and is separate from its suspected effect on proliferation. CD44 knockdown increased the death of detached single cells (anoikis) within 48 hours in suspension (Supplementary Fig. S6F). These data also support the idea that CD44 initiates cellular aggregation and subsequently prevents anoikis during the extended hours and days following detachment and circulation.

Compared with the CD44 wild-type (WT) controls, the CD44 KO cells lost aggregation capacity *in vitro* when measured within 24 hours (Fig. 3J and K). Although the CD44 KO cells showed impaired aggregation as early as 1 hour, they did not show increased cell death compared with WT controls between 1 and 24 hours (Supplementary Fig. S6G and S6H), further confirming that the effect of CD44 on aggregation is in parallel or prior to any potential effects on cell survival. The lost aggregation was restored by overexpression of CD44 in MDA-MB-231 KO cells (Supplementary Fig. S7A–S7C), demonstrating that CD44 is sufficient in mediating cell aggregation.

We proceeded to examine whether CD44 is required for lung colonization of aggregated CTCs *in vivo*. Upon tail-vein infusion, the si*CD44*-transfected TN1 and TN2 PDX tumor cells as well as CD44 KO MDA-MB-231 cells led to a reduced efficiency of lung colonization as measured by bioluminescence imaging (Fig. 4A–F). In a competitive lung colonization assay via tail-vein infusion of MDA-MB-231 cells, single eGFP$^+$ CD44 KO and tdTomato$^+$ CD44 WT cells (mixed at a 1:1 ratio) homed to the lungs in proximity to each other (Fig. 4G, top row). A majority of tdTomato$^+$ CD44 WT cells formed red clusters, whereas most of the eGFP$^+$ CD44 KO cells were single

Downloaded from http://aacrjournals.org/cancerdiscovery/article-pdf/9/1/96/1847835/96.pdf by guest on 27 August 2022

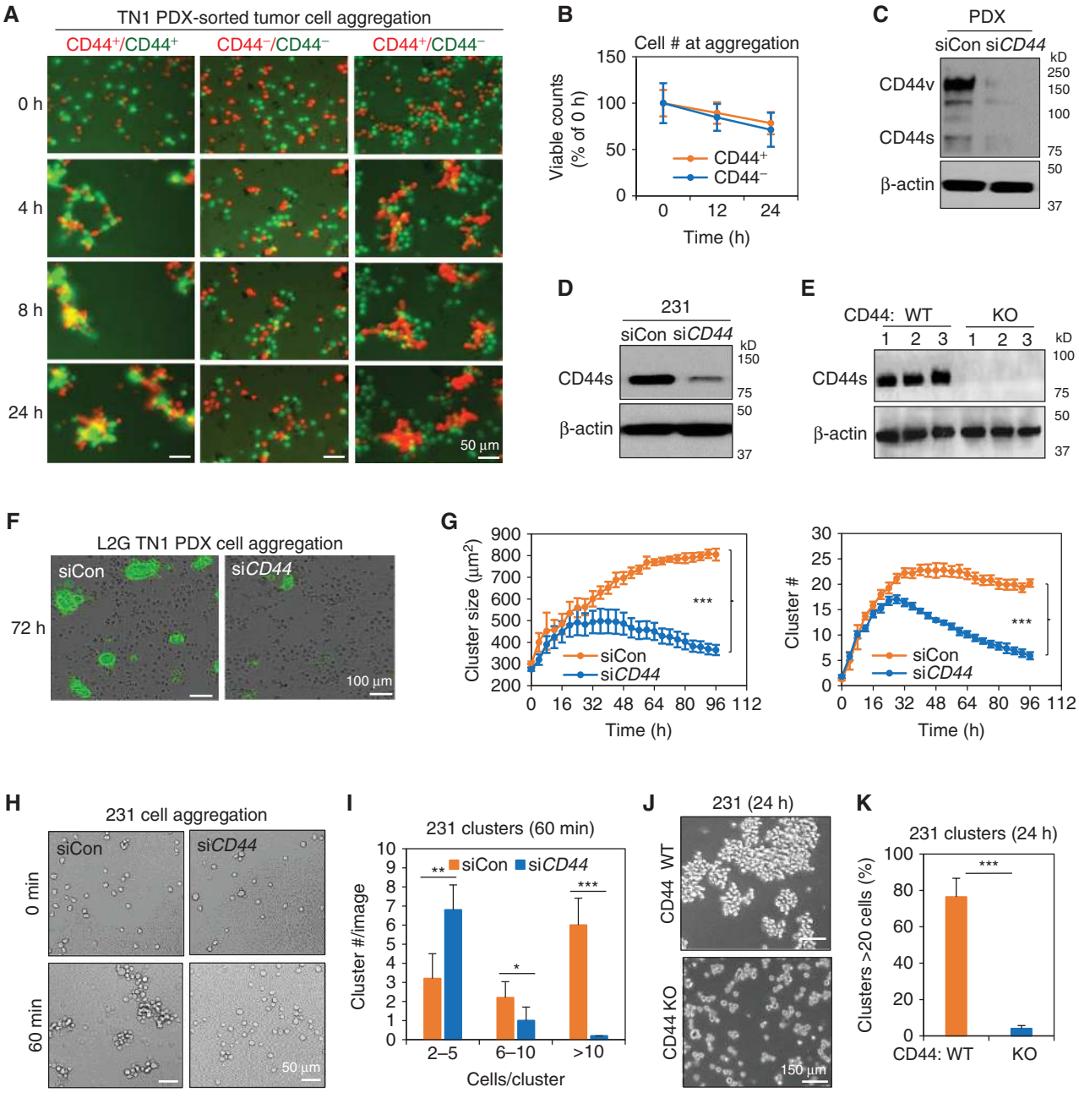

Figure 3. CD44 directs polyclonal tumor cell aggregation. **A,** Time-lapse aggregation images at 0, 4, 8, and 24 hours of incubation with PDX-derived 1:1 mixtures of tdTomato+ and eGFP+ primary tumor cells. Left column, sorted CD44+; middle column, CD44−; right column, mixed CD44+/CD44− cells in two colors. For details, see the Supplementary Videos S6 to S8. **B,** Number of viable CD44+ versus CD44− cells at the time points of 12- and 24-hour aggregation (*t* test $P = 0.6$, $n = 4$). **C,** Immunoblot of CD44 and β-actin (loading control) in TN1 PDX tumor cells upon transfection of the scrambled siRNA control (siCon) or si*CD44*, which caused a depletion of the dominant variant CD44 (CD44v; molecular weight 120–160 kDa) and the marginal standard CD44 (CD44s; molecular weight ~80 kDa). **D,** CD44 immunoblot showing si*CD44*-mediated knockdown of the exclusive CD44s in MDA-MB-231 cells compared with the control (siCon). **E,** CD44 immunoblot of three MDA-MB-231 batches of populations upon CRISPR/Cas9-based CD44 knockout (KO) with gRNA targeting exon 2. **F,** Snapshot images showing reduced aggregation of L2G-labeled TN1 PDX tumor cells at 72-hour clustering time point after si*CD44* and siCon transfections, measured via IncuCyte imaging system. **G,** Quantitative curves of the cluster size (left) and number (right) of TN1 cells measured via IncuCyte time-lapse imaging ($n = 3$ biological replicates, MANOVA ***, $P < 0.001$). **H,** Snapshot images taken at 0 and 60 minutes of MDA-MB-231 suspension cell aggregation onto polyhydroxyethyl methacrylate-treated plates, at 48 hours after si*CD44* and siCon transfections. Scale bars, 50 μm. **I,** Cluster counts of MDA-MB-231 cells at 60-minute aggregation. The data were from at least five images for each group per experiment. The experiments were repeated three times ($n = 3$). *t* test *, $P < 0.05$; **, $P < 0.01$; ***, $P < 0.001$. **J,** Cluster images of CD44 WT and KO (via CRISPR/Cas9) MDA-MB-231 cells at the 24-hour aggregation time point. Scale bars, 150 μm. **K,** Quantitative counts of clustered MDA-MB-231 cells with a cluster size of >20 cells show a significant, dramatic reduction in CD44 KO cells ($n = 5$, *t* test ***, $P < 0.001$).

Downloaded from http://aacrjournals.org/cancerdiscovery/article-pdf/9/1/96/1847835/96.pdf by guest on 27 August 2022

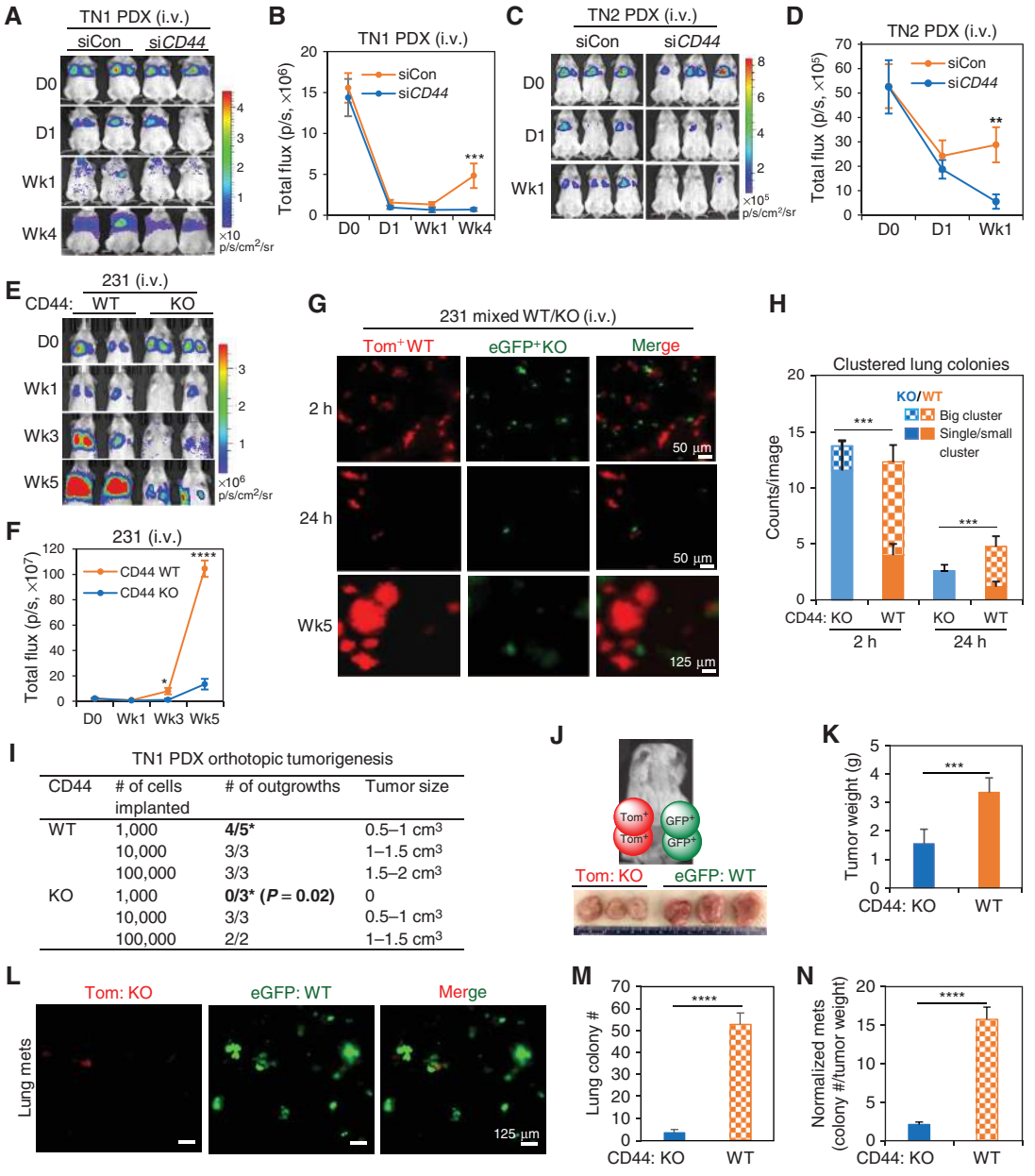

CD44	# of cells implanted	# of outgrowths	Tumor size
WT	1,000	**4/5***	0.5–1 cm³
	10,000	3/3	1–1.5 cm³
	100,000	3/3	1.5–2 cm³
KO	1,000	**0/3* (*P* = 0.02)**	0
	10,000	3/3	0.5–1 cm³
	100,000	2/2	1–1.5 cm³

Figure 4. CD44 depletion blocks tumor cell aggregation and lung metastasis *in vivo*. **A,** Bioluminescence images of lung colonization of the siRNA control (siCon) and si*CD44*-transfected TN1 tumor cells on days 0 (D0) and 1 (D1) and weeks 1 (Wk1) and 4 (Wk4) after tail-vein infusion. Cells (5×10^5) were injected into mice at 36 hours after the initial transfection. **B,** Quantitative bioluminescence signal curves (total flux, p/s) of the TN1 PDXs (siCon and si*CD44*) as measured in **A**, $n = 5$ mice per group. *t* test ***, $P < 0.001$. **C,** Bioluminescence images of lung colonization of the siRNA control (siCon) and si*CD44*-transfected TN2 tumor cells on days 0 (D0) and 1 (D1) and week 1 (Wk1) after tail-vein infusion. Cells (5×10^5) were injected into mice at 36 hours after the initial transfection. **D,** Quantitative bioluminescence signal curves (total flux, p/s) of the TN2 PDXs (siCon and si*CD44*) as measured in **C**; $n = 5$ mice per group. *t* test **, $P < 0.01$. **E,** Bioluminescence images of lung colonization of L2T-labeled CD44 WT and KO MDA-MB-231 tumor cells on day 0 (D0) and weeks 1 (Wk1), 3 (Wk3), and 5 (Wk5) after tail-vein infusion. **F,** Quantitative analyses of the lung bioluminescence signals of CD44 WT and KO cells imaged in **E** ($n = 4$). *t* test *, $P < 0.05$; ****, $P < 0.0001$. **G,** Fluorescence images of the lungs at 2 and 24 hours and 5 weeks after tail-vein infusion of mixed eGFP⁺CD44KO and tdTomato⁺CD44 WT tumor cells (1:1 ratio). Three columns represent the images from the tdTomato channel, the eGFP channel, or the merged channels, respectively. Scale bars, 50 μm for the images taken at 2 and 24 hours, and 125 μm for the images taken at week 5. **H,** Counts of single (solid bar) or clustered tumor cells (checked bar) of CD44 WT and KO cells in the lung images at 2 and 24 hours after tail-vein injections in **E**. At least five lung images were taken for each mouse ($n = 3$ mice). **I,** Tumorigenesis results of PDX-derived CD44 WT and KO cells implanted into the mammary fat pads (second and fourth), from 1,000 to 100,000 cells per injection. *t* test *, $P = 0.02$ between WT/KO implantations of 1,000 cells. **J,** Top, depiction of orthotopic implantation of CD44 WT (eGFP⁺) and KO (tdTomato⁺) tumor cells (100,000 cells per injection) separately into the left and right mammary fat pads of each NOD/SCID mouse. Bottom, images of breast tumors derived from the above implantations at harvest (3 weeks). **K,** Comparison of tumor weight of CD44 WT (eGFP⁺) and KO (tdTomato⁺) tumors derived from 100,000 cell injections in **J** ($n = 6$ mice). *t* test ***, $P < 0.001$. **L,** Fluorescence images, from the channels of tdTomato (left), eGFP (middle), and merged (right), of the dissected lungs with spontaneous metastases (mets) of CD44 WT (eGFP⁺) and KO (tdTomato⁺) tumors, at 3 weeks after orthotopic implantation of these cells into the left and right fourth mammary fat pads, respectively (as shown in **J**). Scale bars, 125 μm. **M** and **N,** Comparison of lung colonies (**M**) and normalized lung metastases (colony # per gram of tumor weight; **N**) following implantations of CD44 WT and KO cells. *t* test ****, $P < 0.0001$.

Downloaded from http://aacrjournals.org/cancerdiscovery/article-pdf/9/1/96/1847835/96.pdf by guest on 27 August 2022

green cells at 2 hours after infusion (Fig. 4G, top row, 4H). By 24 hours after infusion, few eGFP$^+$ CD44 KO cells (~5%) remained detectable, whereas ~30% of tdTomato$^+$ CD44 WT cells were visible under the fluorescence microscope, leading to a significant difference in the long-term (i.e., 5 weeks) colonization efficiency (Fig. 4G, middle and bottom rows, and 4H).

Using the lentiviral CRISPR/Cas9 and CD44 gRNAs, we also transduced CD44$^+$ CSCs from TN1 PDXs and sorted the L2G/L2T-labeled KO cells based on surface CD44 expression and L2G/L2T (Supplementary Fig. S7D). Using sorted CD44 WT and KO cells from PDXs for orthotopic implantations, we detected a reduced tumorigenic potential of CD44 KO PDX tumor cells at a low number of 1,000 cells (Fig. 4I; $P < 0.05$, $n = 5$). Furthermore, on either side of the fourth mammary fat pads of each recipient mouse, we implanted a sufficient number (≥100,000 cells) of tdTomato$^+$ CD44 KO and eGFP$^+$ CD44 WT cells (MDA-MB-231) to enable tumorigenesis into two separate tumors. These mice showed spontaneous lung metastases with a majority of green CD44 WT colonies and very few red CD44 KO colonies (Fig. 4J–N). Although the CD44 KO tumors had a 50% reduction of tumor weight compared with the CD44 WT control tumors (Fig. 4J and K), the normalized number of lung metastatic loci per primary tumor weight of KO cells was only one eighth that of WT cells (Fig. 4L–N). These data strongly suggest that CD44 is required for cluster formation and lung metastasis.

CD44 Mediates Intercellular, Homophilic Protein Interactions in Tumor Cell Aggregates

CD44 is an adhesion molecule and a known receptor for hyaluronic acid (hyaluronan) in lymphocytes (36–38). We initially speculated that hyaluronan binding to CD44 underlies the intercellular interactions of CTC aggregates. However, a hyaluronan antagonist (o-HA, provided by Dr. Bryan P. Toole, Medical University of South Carolina) failed to block TN1 PDX tumor cell aggregation but rather slightly promoted the cluster size of tumor cell aggregates (Fig. 5A and B). Consistently, the hyaluronic acid synthase inhibitor

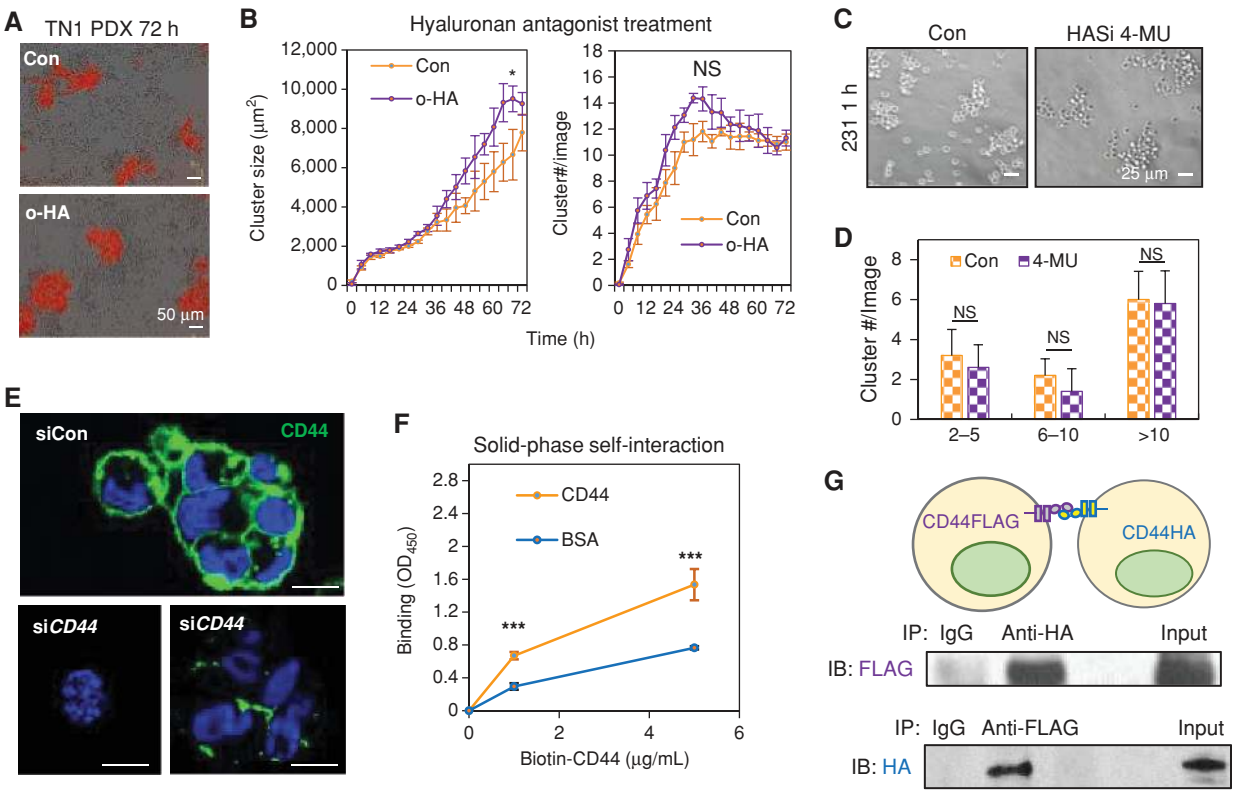

Figure 5. CD44 mediates cell aggregation via intercellular, homophilic interactions. **A,** Aggregation images at the 72-hour time point showing that hyaluronan antagonist (o-HA) slightly increased the cluster size of L2T-labeled TN1 PDX tumor cells. Scale bars, 50 µm. **B,** Quantitative curves of the cluster size (left) and number (right) of TN1 cells measured via IncuCyte time-lapse imaging ($n = 3$ biological replicates; MANOVA *, $P < 0.05$). **C,** Images of MDA-MB-231 cell aggregation at 1 hour with or without hyaluronic acid synthase inhibitor (HASi) 4-MU (at 0.4 mmol/L) pretreatment for 48 hours. Scale bars, 25 µm. **D,** Quantitative counts of aggregated MDA-MB-231 cells with cluster sizes of 2–5, 6–10, and >10 cells pretreated with or without 4-MU ($n = 5$). NS, no significant difference. **E,** CD44 immunofluorescence staining with dissociated MDA-MB-231 cells during the aggregation assay 48 hours after transfection with siCon (top) and si*CD44* (bottom). Most of the CD44-negative cells remained as single cells in suspension, whereas residual CD44 in knockdown cells was located at the intercellular interface of a few clusters. **F,** The binding curves of biotin-conjugated CD44 at 0, 1, and 5 µg/mL to the solid phase CD44 and BSA, measured as OD_{450} units. *t* test ***, $P < 0.001$. **G,** Top, diagram of mixed HEK-293 cell aggregates of two populations transfected with C-terminal FLAG-tagged and HA-tagged CD44, respectively. Bottom, immunoblots for the CD44-FLAG and CD44-HA proteins upon co-IP with anti-HA and anti-FLAG antibodies, respectively. (*continued on next page*)

Downloaded from http://aacrjournals.org/cancerdiscovery/article-pdf/9/1/96/1847835/96.pdf by guest on 27 August 2022

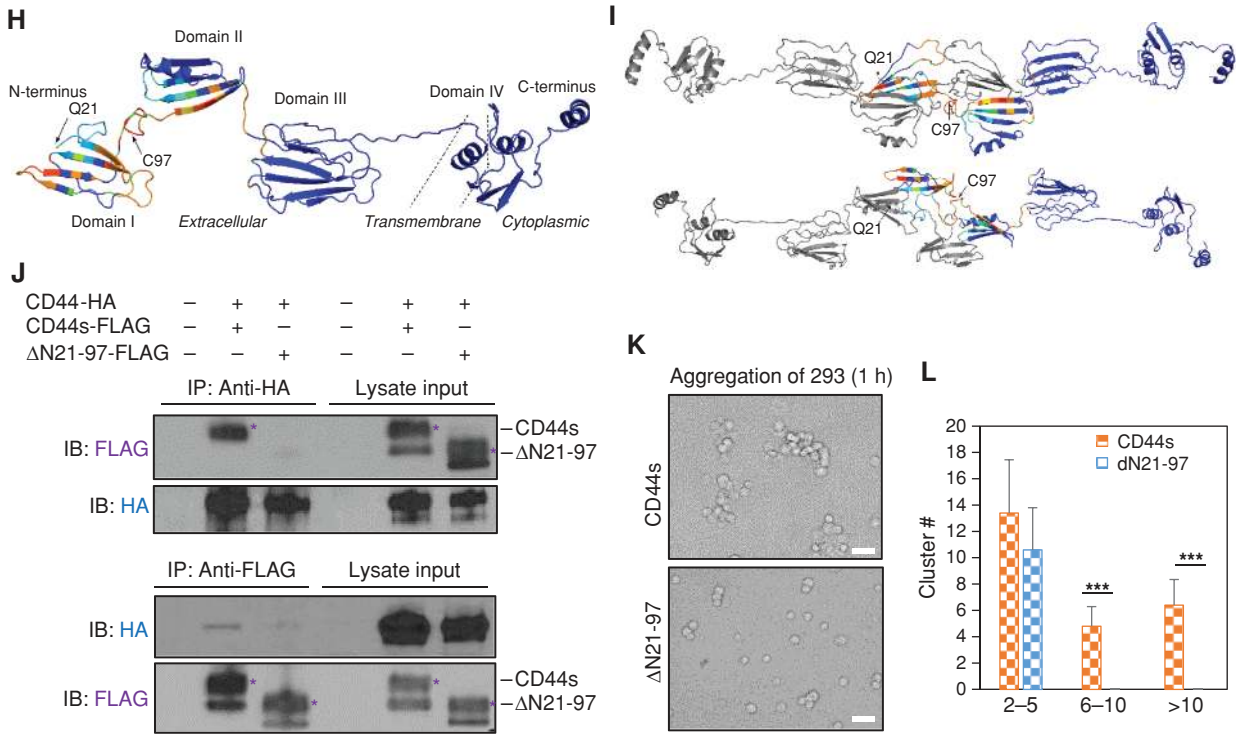

Figure 5. ***(Continued)*** **H,** Structure model of CD44s monomer (the signal peptide 1–20 not shown) with the N-terminal residues, especially Q21-C97 of the extracellular domain I and the beginning of the domain II, as predicted by computational algorithm iTasser. Warmer colors indicate higher probabilities to be at the dimer interface, as predicted by protein docking algorithm BAL. **I,** Two representative structure models (top and bottom) of predicted CD44 homodimers (formed between two neighboring cells) at an almost straight angle from protein docking. The right monomer is color coded in the same way as in **H,** whereas the left one is in gray for contrast (see Supplementary Fig. S8 for additional structure models). **J,** Immunoblots for CD44-FLAG (CD44s and ΔN21-97) and CD44-HA proteins upon co-IP using anti-HA and anti-FLAG antibodies with mixed HEK-293 cell aggregates of two populations transfected with FLAG-tagged (CD44s and ΔN21-97) and HA-tagged CD44, respectively. *, CD44s WT or mutant bands. **K,** Images of aggregation of HEK-293 cells for 1 hour, at 48 hours after transfection with CD44s-FLAG and ΔN21-97-FLAG. Scale bars, 50 μm. **L,** Quantitative counts of aggregated HEK-293 cells, transfected with CD44s-FLAG and ΔN21-97-FLAG, in cluster sizes of 2–5, 6–10, and >10 cells. *t* test ***, $P < 0.001$.

(HASi) 4-MU did not significantly alter the aggregation of MDA-MB-231 cells in suspension (Fig. 5C and D). Therefore, CD44-directed tumor cell aggregation is hyaluronan-independent. To determine whether other adhesion molecules such as E-cadherin are involved in CD44-mediated cell aggregation, we conducted human adhesion molecule antibody array analysis for 17 major adhesion molecules with both CD44 WT and KO cell lysates. However, most of the adhesion molecules were not altered by CD44 KO, and E-cadherin was not detectable in MDA-MB-231 cells (Supplementary Fig. S7E). These data suggest that CD44-mediated tumor cell aggregation is independent of its known ligand hyaluronan, E-cadherin, and other unaltered adhesion molecules.

We subsequently investigated the possibility that CD44 mediates CD44–CD44 homophilic, intercellular interactions within cell aggregates using multiple experimental approaches. Using anti-CD44 immunofluorescence staining, we first found that the residual CD44 protein was mainly located at the interface of a few tumor cell aggregates upon si*CD44* knockdown (Fig. 5E). Second, we performed a solid-phase self-interaction assay *in vitro* with His-tagged CD44 extracellular domain (ExD). CD44 ExD was immobilized to the test plates (solid phase) and displayed a significant binding to biotin-labeled CD44 ExD versus the BSA control (Fig. 5F), demonstrating a homophilic interaction between the CD44 ExDs. Third, we overexpressed CD44 with two different C-terminal tags, CD44-FLAG (standard form CD44s) and CD44-HA (full length), into two separate sets of CD44$^-$ HEK-293 cells. Upon dissociation, CD44-FLAG–expressing cells were then mixed and aggregated with CD44-HA–expressing cells (Fig. 5G, top) prior to harvest and cell lysis for coimmunoprecipitation (co-IP). Notably, the homophilic interactions between intercellular CD44-HA and CD44-FLAG proteins were reciprocally detected via the immunoblotting of CD44-FLAG protein and CD44-HA protein in the separate co-IP pulldown lysates with the anti-HA and the anti-FLAG antibodies, respectively (Fig. 5G, bottom). This demonstrates that intercellular CD44–CD44 interactions are responsible for mediating homophilic tumor cell aggregates.

To further determine the importance of CD44 homophilic interaction in cell aggregation and lung colonization, we analyzed the CD44 sequences and structure models for subsequent studies. Based on the computational analyses and machine learning–assisted modeling, the CD44s monomer shows an elongated four-domain structure with three ExDs (Fig. 5H). The 10 homodimer models of CD44 from multistage protein docking all suggest that the N-terminal domain I (amino acids 21–97) and domain II's first few

Downloaded from http://aacrjournals.org/cancerdiscovery/article-pdf/9/1/96/1847835/96.pdf by guest on 27 August 2022

residues are mainly responsible for the dimerization (Fig. 5I; Supplementary Fig. S8A). To avoid disrupting the stability of domain structures, we therefore truncated domain I (ΔN21-97) for subsequent co-IP and cellular aggregation analyses. Upon transfection into HEK-293 cells, the ΔN21-97 mutant was deficient in forming intercellular complexes with CD44 (Fig. 5J) and lost the capacity of mediating cell aggregation (Fig. 5K and L). The N-terminal domain–dependent CD44 homophilic interaction was also blocked by an anti-CD44 neutralizing antibody when administered to aggregating cells in suspension (Supplementary Fig. S8B). Meanwhile, the treatment of this anti-CD44 antibody inhibited cellular aggregation of MDA-MB-231 breast cancer cells in suspension (Supplementary Fig. S8C and S8D). Upon tail-vein injection, CD44-dependent cluster formation and colonization of TN1 PDX cells and HEK-293 cells within the lungs were further significantly diminished by the anti-CD44 blockade treatment and truncation of the CD44 self-interacting domain (ΔN21-97), respectively (Supplementary Fig. S8E–S8G).

CD44 Maintains PAK2 Levels in Tumor Cell Aggregates

To better understand the CD44-mediated molecular targets and downstream pathways during tumor cell aggregation, we conducted mass spectrometry analyses of sorted $CD44^+$ and $CD44^-$ PDX tumor cells prior to aggregation as well as the CD44 knockdown and control cells after aggregation. We identified 535 proteins and 382 proteins differentially expressed by more than 2-fold in the two comparisons ($CD44^{+/-}$ and siCon/si*CD44*), respectively (Fig. 6A; Supplementary Table S4), including two overlapping signaling pathways: protein ubiquitination and eIF2 signaling (Supplementary Fig. S9A). Out of the 38 overlapping proteins regulated by CD44 in both comparisons, PAK2 was identified as a critical component in four of the top 13 CD44-regulated pathways, such as focal adhesion kinase (FAK) signaling, paxillin signaling, actin cytoskeleton signaling, and TNFR1 signaling (Fig. 6A). PAK2 is a p21-activated kinase that activates the FAK signaling pathway as one of the three members of the evolutionarily conserved group I PAK family of serine/threonine protein kinases, along with PAK1 and PAK3 (26). We further confirmed that si*CD44* transfection reduced PAK2 protein levels in TN1 PDX tumor cells (Fig. 6B) along with decreased FAK protein levels during aggregation (Supplementary Fig. S9B). However, the *PAK2* mRNA levels were unaffected upon CD44 knockdown (Fig. 6C). Although FAK had been reported to promote breast cancer stemness (39, 40), the pluripotency marker OCT3/4 levels were also reduced in CD44 KO cells compared with the WT MDA-MB-231 cells (Supplementary Fig. S9C), suggesting that CD44 depletion impairs cancer stemness.

To determine the importance of PAK2 in tumor cell aggregation and lung metastasis, we inhibited PAK activity using a chemical inhibitor and then knocked down its expression via siRNAs in multiple tumor cells. We found that the PAK inhibitor FRAX597 partially blocked the *ex vivo* aggregation of TN1 PDX tumor cells (Supplementary Fig. S9D and S9E). We further investigated the specific effects of knocking down PAK2 on cell aggregation of PDXs and MDA-MB-231 cells. Comparable to the cluster blocking effects of si*CD44*, si*PAK2*-mediated knockdowns showed an inhibitory effect on TN1 PDX tumor cell aggregation (Fig. 6D and E). Coinciding with that, the pooled and individual *PAK2* siRNAs dramatically inhibited the aggregation of MDA-MB-231 cells in suspension (Supplementary Fig. S9F and S9G), without compromising the cell survival at the 24-hour time point of aggregation (Supplementary Fig. S9H). Furthermore, the si*PAK2* knockdown mimicked si*CD44* in blocking the TN1 PDX tumor cell–mediated lung colonization in NSG mice (Fig. 6F and G), suggesting that PAK2 significantly contributes to CD44-mediated tumor cell aggregation and lung metastasis.

We then investigated the molecular mechanism by which CD44 regulates or sustains PAK2 protein levels. Considering that the *PAK2* mRNA levels were not altered upon CD44 depletion (Fig. 6C), we hypothesized that CD44 regulates PAK2 at posttranscriptional levels, especially at protein levels. We first detected protein interactions between endogenous CD44 and PAK2 using co-IP with the lysates of aggregated MDA-MB-231 cells (Supplementary Fig. S9I). Then we confirmed the CD44–PAK2 protein complex formation using co-IP with 293 cell aggregates expressing tagged PAK2-FLAG and CD44-HA (Fig. 6H). Lastly, based on the immunofluorescence staining of MDA-MB-231 tumor cells, endogenous CD44 and PAK2 were observed to colocalize at the plasma membrane of aggregated cells (Fig. 6I), whereas in single cells, CD44 and PAK2 failed to colocalize but with a coincident reduction of both protein levels (Fig. 6I, white arrow).

To determine the downstream signaling effects of PAK2 interaction with CD44, we knocked down PAK2 in breast tumor cells and found that si*PAK2* mimicked si*CD44* transfection in decreasing the FAK protein levels as well as FAK activation and phosphorylation (Fig. 6J). Surprisingly, PAK2 knockdown also decreased CD44 protein levels in the tumor cells (Fig. 6J), suggesting positive feedback and promotion between CD44 and PAK2, likely through protein complex–mediated stabilization of both proteins.

Human $CD44^+$ CTC Clusters Associated with Clinical Outcomes

We next examined the clinical impact of CD44-mediated breast tumor aggregation and metastasis. Using PrognoScan (41) analyses, we observed that high levels of *CD44* mRNA expression in breast tumors are associated with poor overall survival (OS), relapse-free survival (RFS), and distant metastasis–free survival (DMFS) of patients (Fig. 7A–C; Supplementary Table S5). Consistently, high levels of *PAK2* mRNA expression coincided with poor DMFS of patients with breast cancer (Fig. 7D; Supplementary Table S5). Taking advantage of the CellSearch platform–based blood analysis in patients with breast cancer, we confirmed the worse OS of patients with detectable CTC clusters versus the patients with single CTCs only (Fig. 7E; Supplementary Table S6; $n = 118$ patients with metastatic breast cancer). We also found that $CD44^+$ CTC clusters in human blood were associated with lower OS than $CD44^-$ CTCs (Fig. 7F and G; Supplementary Table S7).

Overall, these results identify cellular aggregation of individually migrating and circulating tumor cells as a new mechanism of tumor cell cluster formation in breast cancer, which

Downloaded from http://aacrjournals.org/cancerdiscovery/article-pdf/9/1/96/1847835/96.pdf by guest on 27 August 2022

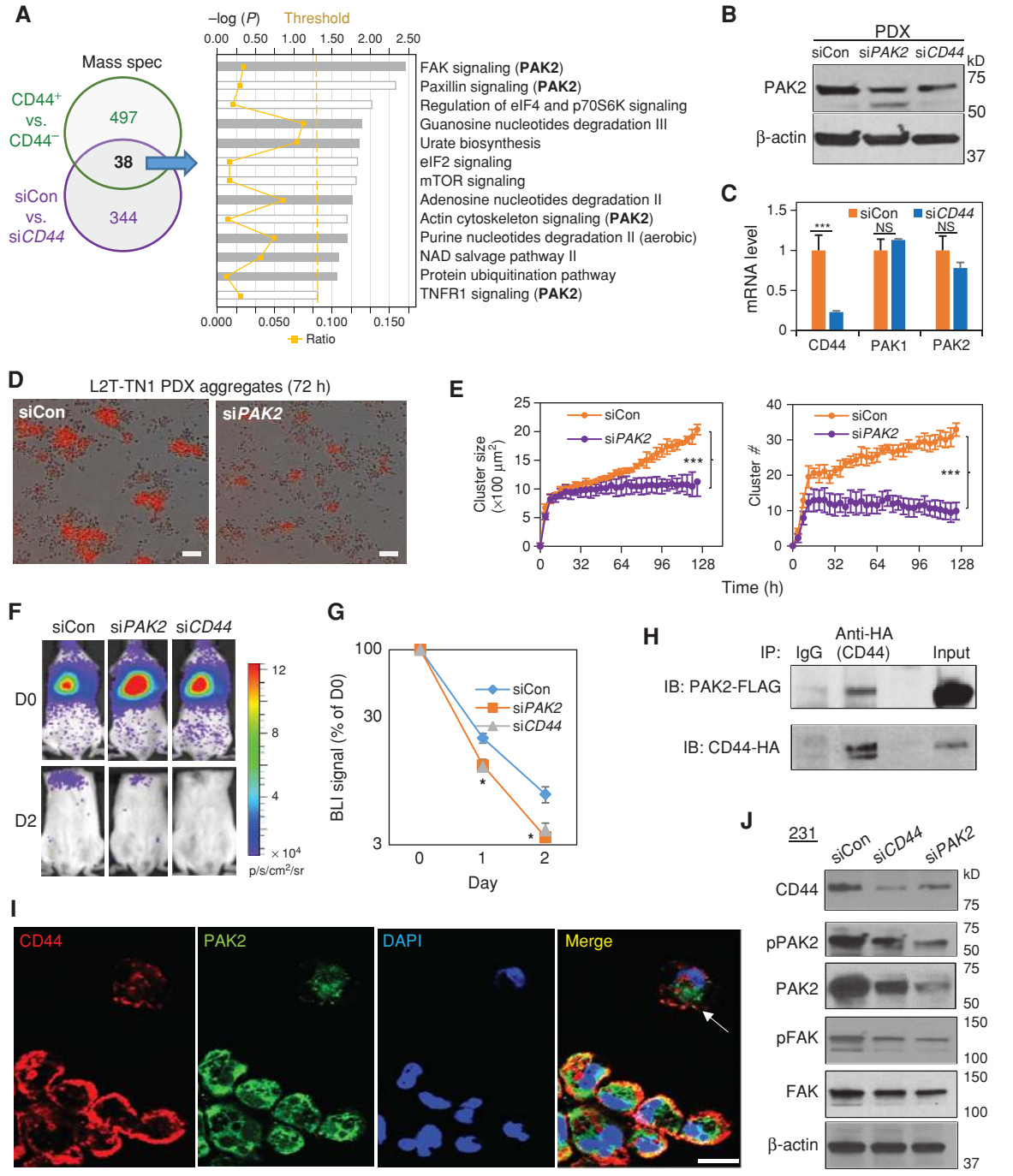

Figure 6. CD44 promotes the PAK2 pathway in tumor cell aggregates. **A,** The number of proteins with a >2-fold change in CD44⁺ versus CD44⁻ and si*CD44* versus control comparisons: 535 of 1,377, and 382 of 1,523, respectively, with 38 proteins in common. The graph shows the canonical pathways of the 38 overlapped proteins. **B,** Immunoblots of PAK2 in TN1 PDX tumor cells transfected with the control siCon, si*PAK2*, and si*CD44*, at 36 hours after knockdown. Loading control: β-actin. **C,** Relative similar mRNA levels of PAK1 and PAK2 (NS, no significant change) upon si*CD44* knockdown (***, $P < 0.001$), measured via quantitative real-time PCR. **D,** Representative aggregate images of tdTomato⁺ TN1 PDX tumor cells at 72-hour aggregation upon PAK2 knockdown via si*PAK2*. Scale bars, 50 μm. **E,** Quantitative analyses of cluster size (left) and number (right) of TN PDX tumor clusters upon si*PAK2* knockdown, measured by IncuCyte time-lapse imaging. MANOVA ***, $P < 0.001$. **F,** Bioluminescence images of lung colonization of the siCon, si*PAK2*, and si*CD44*-transfected TN PDX tumor cells on days 0 (D0) and 2 (D2) after tail-vein infusion (36 hours after transfection). **G,** Quantitative bioluminescence signal curves (% of D0 signal) of reduced lung colonization of TN PDX cells upon knockdown via si*PAK2* and si*CD44* ($n = 5$ mice per group). *t* test *, $P < 0.05$ for both si*PAK2* and si*CD44* comparisons to the control siCon at both D1 and D2. **H,** Immunoblots for the tagged proteins PAK2-FLAG and CD44-HA upon co-IP with anti-HA (CD44) using the lysates of 293T cell aggregates, 48 hours after cotransfection with PAK2-FLAG and CD44-HA. **I,** IF staining images of endogenous CD44 and PAK2, and DAPI signals showing the high expression of colocalized CD44 and PAK2 at the cytoplasmic membrane of the aggregated MDA-MB-231 cells (24-hour aggregation). In contrast, the single cell (white arrow) in suspension displays low levels of CD44 and PAK2, which are not colocalized. Scale bar, 20 μm. **J,** Immunoblots with MDA-MB-231 cell lysates for CD44, pPAK2, PAK2, pFAK, and FAK detection at 48 hours after transfection with si*CD44* and si*PAK2*. CD44 and PAK2 positively promote each other's protein levels and FAK phosphorylation.

Downloaded from http://aacrjournals.org/cancerdiscovery/article-pdf/9/1/96/1847835/96.pdf by guest on 27 August 2022

is directly mediated by intercellular CD44–CD44 homophilic interactions and dependent on CD44–PAK2 complex–activated downstream pathways (such as FAK and OCT3/4) to promote cancer stemness and metastasis (Fig. 7H).

DISCUSSION

Taken together, our studies demonstrate a novel mechanism of human tumor cluster formation via CD44/PAK2-mediated cellular aggregation using representative PDX models and cell lines in combination with clinical studies.

Within the past decade, CTC analyses have become an important real-time approach for cancer diagnostic and prognostic studies. Multiple technologies have been developed for CTC detection and analysis (e.g., microchip-based capture) and have greatly advanced our understanding of the polyclonal biology of tumor metastasis (42–45). Polyclonal tumor cell clusters have also been detected in additional solid tumors such as pancreatic cancer (46). Our study has unveiled the dynamics of cellular migration and aggregation leading to tumor cell cluster formation prior to and after intravasation. We propose that this new mechanism may

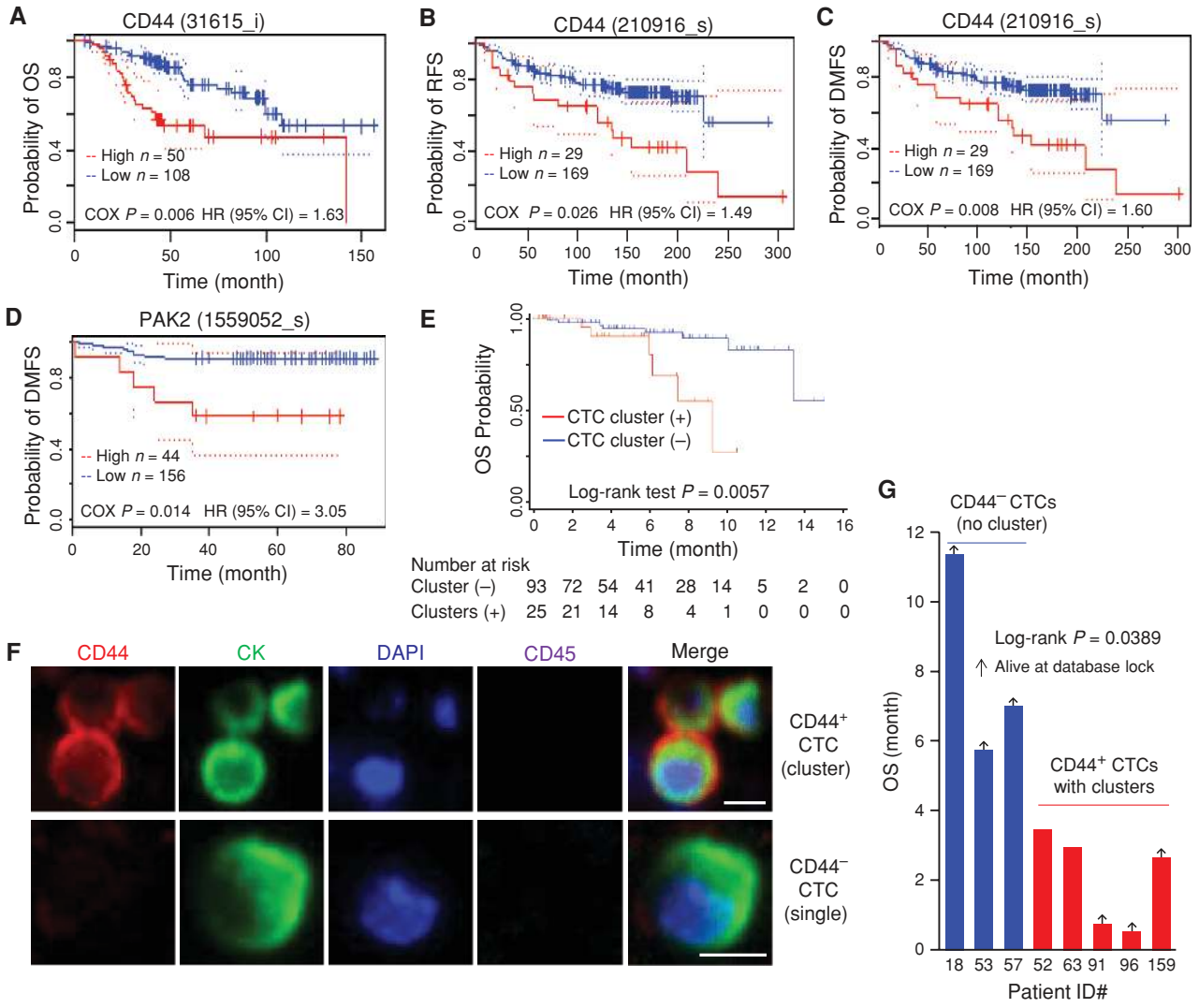

Figure 7. CD44+ CTC cluster association with clinical outcomes. **A–C,** Kaplan–Meier plot of OS (**A**), RFS (**B**), and DMFS (**C**) for patients with high (red) and low (blue) CD44 (probes 31615_i or 210916_s) expression in breast tumors. Expression was dichotomized at the optimal cutoff point plotted in GSE3143 ($n = 158$, left) and GSE7390 ($n = 198$, right two plots). 95% confidence intervals for each group are indicated by dotted lines. Cox $P = 0.006$, 0.026, and 0.008 as indicated. **D,** Kaplan–Meier plot of DMFS by *PAK2* mRNA expression. High (red) and low (blue) groups were determined using the optimal cutoff point in the GSE19615 human breast tumor database ($n = 200$). Cox $P = 0.014$. **E,** Kaplan–Meier plot of OS for Northwestern patients with breast cancer with cluster-positive and cluster-negative CTCs, detected by CellSearch ($n = 118$, log-rank test $P = 0.0057$; Supplementary Table S6). **F,** Representative images of a CD44+ cell cluster (top plots) and a single CD44– CTC (bottom) detected in human peripheral blood via CellSearch platform staining for CD45, CD44, CK, and DAPI. Scale bar, 10 μm. **G,** Bar graph of OS, based on the swimmer plot principle, for Northwestern patients with breast cancer with CellSearch-detected CD44+ CTC clusters and CD44– CTCs only ($n = 8$, log-rank test $P = 0.0389$). Two patients with CD44+ clusters were deceased due to disease progression (Supplementary Table S7). (*continued on next page*)

Downloaded from http://aacrjournals.org/cancerdiscovery/article-pdf/9/1/96/1847835/96.pdf by guest on 27 August 2022

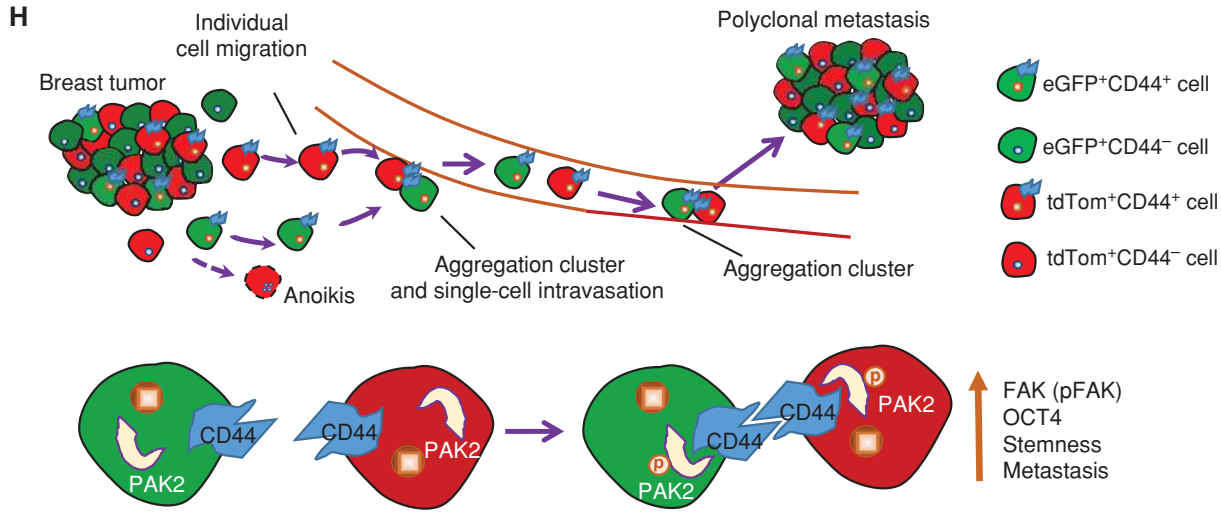

Figure 7. ***(Continued)*** **H,** Diagram of individual cell migration leading to perivascular cluster formation and intravasation. Tumor cells individually migrate to sites of intravasation on blood vessels, where CD44 mediates intercellular, homophilic protein complex formation and subsequent CD44–PAK2 interaction and FAK pathway activation. The self-interaction drives tumor cell aggregation at and within the vasculature in the primary tumor and lung metastases, due to their physical proximity. CD44 directs aggregation of detached breast tumor cells that mediate polyclonal metastasis, while single CD44⁻ tumor cells undergo anoikis within 48 to 72 hours of detachment.

act in addition to the previously proposed model of collective migration and cohesive shedding of polyclonal CTC clusters (5, 28, 47) and that there may be a possible interplay or synergy between the two mechanisms in cluster formation and transportation. The retention of CTC clusters in the capillaries of distant organs may be capable of stopping blood flow and generating a new microenvironmental niche for metastatic tumor regeneration. It is also possible for CTC clusters to reversibly break down into individual cells prior to extravasation, similar to the process of individual cell departure from clusters with subsequent intravasation. An *in vitro* study using microfluidic devices designed to mimic human capillary constrictions indicated that CTC clusters have the ability to dynamically break down and reform cell–cell junctions and traverse capillary-sized vessels (48).

Our studies suggest a new mechanism of homophilic interactions by which the CSC marker CD44 directs CTC aggregation to promote polyclonal metastasis. CD44 is known to bind to its ligand hyaluronan in lymphocytes; however, CD44-mediated tumor cell aggregation is independent of the hyaluronan-ligand binding, but is mediated by its intercellular, homophilic interactions, similar to other adhesion molecules such as E-cadherin (49) and PECAM1 (50). Notably, the N-terminal domain responsible for CD44 homophilic interactions also harbors most of the known hyaluronan-binding sites (51). Although E-cadherin and other tight junction components mediate collective migration of tumor cell clusters (5, 28), CD44-mediated cell aggregation to form tumor cell clusters is E-cadherin independent and occurs through a distinct pathway that interacts with and activates PAK2 kinase and subsequently FAK signaling. Although FAK is known to play an important role in CSCs and cancer progression (39, 40), PAK2 is relatively less studied. Limited studies have reported that mouse *Pak2* KO results in embryonic lethality with impaired somite development and growth retardation (52). Murine PAK2 and its kinase activity are required for homing of hematopoietic stem and progenitor cells to the bone marrow (53). Human PAK2 regulates apoptosis (54) and drives tamoxifen resistance in breast cancer (55). All of these implicate a pivotal role of PAK2 in normal stem-cell functions and cancer progression. Our studies further demonstrate the role of PAK2 in tumor cell aggregation and CSC-mediated metastasis.

Our work indicates that the high efficiency of CTC clusters in mediating metastasis is due not only to their advantageous survival, but also to their CSC properties and CD44-mediated signaling pathways. We propose that the increased stemness of clusters enables their plasticity and regenerative potential (32, 33), leading to enhanced adaptation to new microenvironments and improved secondary tumor growth. Although CTCs provide advantages for noninvasive dynamic monitoring of cancer progression, the understanding of the stemness and molecular mechanisms of CTC clusters will also improve both diagnostic prediction and development of therapeutics that prevent and block polyclonal metastasis. Regardless, our results show that CD44-mediated cell aggregation can, in parallel or subsequently, promote cell survival, which is certainly required for CSC functions such as self-renewal and metastasis. Future studies may address how CTC clusters cross-talk with other blood cells such as macrophages (56) and platelets (57) in metastasis.

METHODS

Human Specimen Analyses

All human blood and tumor specimen analyses complied with NIH guidelines for human subject studies and were approved by the Institutional Review Boards at Northwestern University and Case Western Reserve University/University Hospitals. The investigators obtained informed written consent from all subjects whose blood

Downloaded from http://aacrjournals.org/cancerdiscovery/article-pdf/9/1/96/1847835/96.pdf by guest on 27 August 2022

specimens were analyzed. Consent was waived for the IHC staining of archived tumor specimens.

Animal Studies

All mice used in this study were kept in specific pathogen-free facilities in the Animal Resources Center at Northwestern University, Case Western Reserve University, and Albert Einstein College of Medicine. All animal procedures complied with the NIH Guidelines for the Care and Use of Laboratory Animals and were approved by the respective Institutional Animal Care and Use Committees. Animals were randomized by age and weight. The exclusion criterion of mice from experiments was sickness or conditions unrelated to tumors. Sample sizes were determined based on the results of preliminary experiments, and no statistical method was used to predetermine sample size. All of the PDX tumors were established, and orthotopic tumor implantation was performed as described previously (9, 17).

Cell Lines and Transfections

MDA-MB-231 and HEK-293 cells were purchased commercially from ATCC, and periodically verified to be *Mycoplasma*-negative using Lonza's MycoAlert Mycoplasma Detection Kit (cat #LT07-218). Cell morphology, growth characteristics, and microarray gene-expression analyses were compared with published information to ensure their authenticity. Early passage of cells (<20 passages) was maintained in DMEM with 10% FBS + 1% penicillin–streptomycin (P/S). Primary tumor cells were cultured in HuMEC-ready medium (Life Technologies) plus 5% FBS and 0.5% P/S in collagen type I (BD Biosciences) coated plates. miRNAs (Dharmacon, negative control #4) and siRNAs (pooled; Dharmacon, negative control A) were transfected using Dharmafect (Dharmacon) at 100 nmol/L, and retransfected on the following day. For overexpression experiments in HEK-293 cells, pCMV6-FLAG-CD44 (OriGene), pCMV3-HA-CD44, pCMV3-FLAG-PAK2, and pCMV3-HA-PAK2 (Sino Biological) plasmids were transfected into cells by PolyJet (SignaGen Laboratories). After 48 hours, cells were collected for co-IP and western blotting.

CD44 Structure Modeling

A three-dimensional structure model of CD44 antigen isoform 4 precursor (CD44s; https://www.ncbi.nlm.nih.gov/protein/48255941) was first built using the webserver iTasser (58). Two copies of CD44s monomer models were rigidly docked into each other using the webserver ClusPro (59) under the homodimer mode. The top 10 distinct homodimer models were then subject to flexible refinement using a Bayesian active learning (BAL) method where the direction and the extent of backbone conformational flexibility are sampled with protein complex–based normal mode analysis cNMA (60, 61). The 10 refined models were reranked with BAL-determined probabilities as weights. Moreover, residues were also assigned probabilities based on the weighted models. Specifically, each residue in each model was assigned the model's probability if it is at the model's putative interface (defined by a 5-Å distance cutoff between homodimeric heavy atom pairs) and a zero otherwise, and each residue had these values across all 10 models summed into the residue's probability ranging from 0 to 1. For instance, if a residue appears at the putative interface of all 10 distinct models, its probability score will be 1. Due to the symmetry of the homodimer, each residue's probability is further averaged over both chains in this study. Structure models were visualized using the molecular graphics program PyMol (62). The predicted "hotspot" residues are concentrated over the first 97 residues where C97 at the first interdomain linker is suggested to form disulfide bonds across some predicted dimer interfaces. As protein docking was performed without the environment of the membrane, the first two homodimer models in Fig. 5I feature an almost straight angle between the two monomers, which would need drastic interdomain conformational changes to accommodate middle domains in a membrane. The alternate two models in Supplementary Fig. S8A forming such an acute angle would not have to do so and are potentially more likely.

Statistical Analysis

For all assays and analyses *in vitro*, if not specified a two-tailed Student *t* test performed using Microsoft Excel was used to evaluate the *P* values, and $P < 0.05$ was considered statistically significant. Data are presented as mean ± standard deviation (SD). For all the IncuCyte clustering assays, biological triplicates were performed. For all other cell-based *in vitro* experiments, three technical replicates were analyzed. For animal studies *in vivo*, cluster curves were analyzed using Wilcoxon rank sum tests and MANOVA analyses in R software. For the fluorescence lung imaging, at least 5 random fields of the lung from each mouse were taken, and at least 3 mice were used. Spearman–Brown reliability coefficients were calculated for a varying number of repeats in order to find the number of technical replicates required to attain a reliability of 90% (63, 64). For animal studies, we determined the group size using Bonferroni correction for multiplicity; we set $\alpha = 0.05/4 = 0.0125$. We assumed the mean difference between the groups was at least twice as much as the SD (effect size = 2.0). For clinical association studies, please refer to Supplementary Methods.

Details Included in the Supplementary Methods

Supplementary Methods include mouse models and tumor dissociation, intravital imaging, bioluminescence imaging, blood collection and CTC analysis, invasive cell collection *in vivo*, cell culture and transfections, CD44 knockout using CRISPR/Cas9 technology, flow cytometry and cell sorting, cell clustering assay, mammosphere assay, lung imaging, RNA extraction and real-time PCR, mass spectrometry, anoikis assay, western blotting, IHC, immunofluorescence, clinical outcome association analysis, statistical analysis, and data availability.

Disclosure of Potential Conflicts of Interest

A.S. Harney is a senior research scientist at Array BioPharma. M. Cristofanilli reports receiving commercial research grants from Pfizer, Novartis, and Merus. J.S. Condeelis is a consultant/advisory board member for MetaStat Inc. and Deciphera Pharmaceuticals. No potential conflicts of interest were disclosed by the other authors.

Authors' Contributions

Conception and design: X. Liu, R. Taftaf, Y. Cao, Y. Shen, D.W. Abbott, J.S. Condeelis, H. Liu

Development of methodology: X. Liu, R. Taftaf, M. Kawaguchi, W. Chen, D. Entenberg, S.M. Chirieleison, Y. Cao, Y. Shen, D.W. Abbott, J.S. Condeelis, H. Liu

Acquisition of data (provided animals, acquired and managed patients, provided facilities, etc.): X. Liu, R. Taftaf, M. Kawaguchi, Y.-F. Chang, W. Chen, D. Entenberg, Y. Zhang, L. Gerratana, S. Huang, D.B. Patel, E. Tsui, S.M. Chirieleison, Y. Cao, A.S. Harney, A. Patsialou, Y. Shen, S. Avril, H.L. Gilmore, J.D. Lathia, M. Cristofanilli, J.S. Condeelis

Analysis and interpretation of data (e.g., statistical analysis, biostatistics, computational analysis): X. Liu, R. Taftaf, M. Kawaguchi, W. Chen, D. Entenberg, Y. Zhang, L. Gerratana, S. Huang, E. Tsui, Y. Cao, S. Patel, Y. Shen, S. Avril, J.D. Lathia, M. Cristofanilli, J.S. Condeelis, H. Liu

Writing, review, and/or revision of the manuscript: X. Liu, R. Taftaf, D. Entenberg, L. Gerratana, S. Huang, S.M. Chirieleison, A.S. Harney, Y. Shen, S. Avril, J.D. Lathia, D.W. Abbott, M. Cristofanilli, J.S. Condeelis, H. Liu

Administrative, technical, or material support (i.e., reporting or organizing data, constructing databases): D.B. Patel, E. Tsui, V. Adorno-Cruz, S. Patel, J.S. Condeelis

Study supervision: J.S. Condeelis, H. Liu

Downloaded from http://aacrjournals.org/cancerdiscovery/article-pdf/9/1/96/1847835/96.pdf by guest on 27 August 2022

Acknowledgments

We appreciate the suggestions and help of Drs. Daniel Haber, Ruth Keri, Bryan P. Toole, Jeremy Rich, David Gius, Shideng Bao, George Stark, Zhenghe Wang, Stanton Gerson, Sanford Markowitz, and Mark Jackson during manuscript preparation and thank them for access to their research resources. We received technical help from Jay T. Myers, Bryson Benjamin, James Hale, and Luke Torre-Healy in addition to all members of the Liu laboratory (especially Andrew Hoffmann, Yuzhi Jia, Beijie Yu, and Nahun Ha). We appreciate the support of the Animal, Imaging, Microscopy, Proteomics, and Flow Core Facilities of Case Western Reserve University, Cleveland Clinic Foundation, and Northwestern University. This article has been partially supported by NIH/NCI grants R00CA160638 (H. Liu), CA150344 (J.S. Condeelis), CA100324 (J.S. Condeelis), and CA216248 (J.S. Condeelis); NIH/NIGMS grant R35GM124952 (Y. Shen); American Cancer Society grant ACS127951-RSG-15-025-01-CSM (H. Liu); the Susan G. Komen Foundation CCR15332826 (H. Liu) and CCR18548501 (H. Liu); the Department of Defense W81XWH-16-1-0021 (H. Liu); Ohio Cancer Research Associates (H. Liu); Case Comprehensive Cancer Center (NCIP30 CA043703 Pilot Grant); Case Western Reserve University and Northwestern University start-up grants (H. Liu); the Albert Einstein College of Medicine Gruss Lipper Biophotonics Center and its Integrated Imaging Program (J.S. Condeelis and D. Entenberg); the Lynn Sage Cancer Research Foundation (X. Liu, M. Cristofanilli, and H. Liu) and Case Western Reserve University CTSA/KL2 TR0002547 (S. Avril).

Received January 22, 2018; revised August 11, 2018; accepted October 17, 2018; published first October 25, 2018.

REFERENCES

1. Poste G, Fidler IJ. The pathogenesis of cancer metastasis. Nature 1980;283:139–46.
2. Chambers AF, Groom AC, MacDonald IC. Dissemination and growth of cancer cells in metastatic sites. Nat Rev 2002;2:563–72.
3. Gupta GP, Massague J. Cancer metastasis: building a framework. Cell 2006;127:679–95.
4. Mu Z, Wang C, Ye Z, Austin L, Civan J, Hyslop T, et al. Prospective assessment of the prognostic value of circulating tumor cells and their clusters in patients with advanced-stage breast cancer. Breast Cancer Res Treat 2015;154:563–71.
5. Aceto N, Bardia A, Miyamoto DT, Donaldson MC, Wittner BS, Spencer JA, et al. Circulating tumor cell clusters are oligoclonal precursors of breast cancer metastasis. Cell 2014;158:1110–22.
6. Bonnet D, Dick JE. Human acute myeloid leukemia is organized as a hierarchy that originates from a primitive hematopoietic cell. Nat Med 1997;3:730–7.
7. Kreso A, Dick JE. Evolution of the cancer stem cell model. Cell Stem Cell 2014;14:275–91.
8. Lapidot T, Sirard C, Vormoor J, Murdoch B, Hoang T, Caceres-Cortes J, et al. A cell initiating human acute myeloid leukaemia after transplantation into SCID mice. Nature 1994;367:645–8.
9. Al-Hajj M, Wicha MS, Benito-Hernandez A, Morrison SJ, Clarke MF. Prospective identification of tumorigenic breast cancer cells. Proc Natl Acad Sci U S A 2003;100:3983–8.
10. Diehn M, Cho RW, Lobo NA, Kalisky T, Dorie MJ, Kulp AN, et al. Association of reactive oxygen species levels and radioresistance in cancer stem cells. Nature 2009;458:780–3.
11. Chao MP, Alizadeh AA, Tang C, Myklebust JH, Varghese B, Gill S, et al. Anti-CD47 antibody synergizes with rituximab to promote phagocytosis and eradicate non-Hodgkin lymphoma. Cell 2010;142: 699–713
12. Jaiswal S, Jamieson CH, Pang WW, Park CY, Chao MP, Majeti R, et al. CD47 is upregulated on circulating hematopoietic stem cells and leukemia cells to avoid phagocytosis. Cell 2009;138:271–85
13. Bao S, Wu Q, McLendon RE, Hao Y, Shi Q, Hjelmeland AB, et al. Glioma stem cells promote radioresistance by preferential activation of the DNA damage response. Nature 2006;444:756–60.
14. Eyler CE, Rich JN. Survival of the fittest: cancer stem cells in therapeutic resistance and angiogenesis. J Clin Oncol 2008;26:2839–45.
15. Chen J, Li Y, Yu TS, McKay RM, Burns DK, Kernie SG, et al. A restricted cell population propagates glioblastoma growth after chemotherapy. Nature 2012;488:522–6.
16. Kurtova AV, Xiao J, Mo Q, Pazhanisamy S, Krasnow R, Lerner SP, et al. Blocking PGE2-induced tumour repopulation abrogates bladder cancer chemoresistance. Nature 2015;517:209–13.
17. Liu H, Patel MR, Prescher JA, Patsialou A, Qian D, Lin J, et al. Cancer stem cells from human breast tumors are involved in spontaneous metastases in orthotopic mouse models. Proc Natl Acad Sci U S A 2010;107:18115–20.
18. Godar S, Ince TA, Bell GW, Feldser D, Donaher JL, Bergh J, et al. Growth-inhibitory and tumor- suppressive functions of p53 depend on its repression of CD44 expression. Cell 2008;134:62–73.
19. Mani SA, Guo W, Liao MJ, Eaton EN, Ayyanan A, Zhou AY, et al. The epithelial-mesenchymal transition generates cells with properties of stem cells. Cell 2008;133:704–15.
20. Dalerba P, Dylla SJ, Park IK, Liu R, Wang X, Cho RW, et al. Phenotypic characterization of human colorectal cancer stem cells. Proc Natl Acad Sci U S A 2007;104:10158–63.
21. Prince ME, Sivanandan R, Kaczorowski A, Wolf GT, Kaplan MJ, Dalerba P, et al. Identification of a subpopulation of cells with cancer stem cell properties in head and neck squamous cell carcinoma. Proc Natl Acad Sci U S A 2007;104:973–8.
22. Li C, Heidt DG, Dalerba P, Burant CF, Zhang L, Adsay V, et al. Identification of pancreatic cancer stem cells. Cancer Res 2007;67:1030–7.
23. Bockhorn J, Prat A, Chang YF, Liu X, Huang S, Shang M, et al. Differentiation and loss of malignant character of spontaneous pulmonary metastases in patient-derived breast cancer models. Cancer Res 2014;74:7406–17.
24. Patsialou A, Bravo-Cordero JJ, Wang Y, Entenberg D, Liu H, Clarke M, et al. Intravital multiphoton imaging reveals multicellular streaming as a crucial component of in vivo cell migration in human breast tumors. Intravital 2013;2:e25294.
25. Harney AS, Arwert EN, Entenberg D, Wang Y, Guo P, Qian BZ, et al. Real-time imaging reveals local, transient vascular permeability, and tumor cell intravasation stimulated by TIE2hi macrophage-derived VEGFA. Cancer Discov 2015;5:932–43.
26. Kumar A, Molli PR, Pakala SB, Bui Nguyen TM, Rayala SK, Kumar R. PAK thread from amoeba to mammals. J Cell Biochem 2009;107:579–85.
27. Alix-Panabieres C, Pantel K. Challenges in circulating tumour cell research. Nat Rev 2014;14:623–31.
28. Cheung KJ, Padmanaban V, Silvestri V, Schipper K, Cohen JD, Fairchild AN, et al. Polyclonal breast cancer metastases arise from collective dissemination of keratin 14-expressing tumor cell clusters. Proc Natl Acad Sci U S A 2016;113:E854–63.
29. Wyckoff JB, Wang Y, Lin EY, Li JF, Goswami S, Stanley ER, et al. Direct visualization of macrophage-assisted tumor cell intravasation in mammary tumors. Cancer Res 2007;67:2649–56.
30. Williams JK, Entenberg D, Wang Y, Avivar-Valderas A, Padgen M, Clark A, et al. Validation of a device for the active manipulation of the tumor microenvironment during intravital imaging. Intravital 2016;5:pii:e1182271.
31. Yu M, Bardia A, Wittner BS, Stott SL, Smas ME, Ting DT, et al. Circulating breast tumor cells exhibit dynamic changes in epithelial and mesenchymal composition. Science 2013;339:580–4.
32. Ramos EK, Hoffmann AD, Gerson SL, Liu H. New opportunities and challenges to defeat cancer stem cells. Trends Cancer 2017;3:780–96.
33. Dashzeveg NK, Taftaf R, Ramos EK, Torre-Healy L, Chumakova A, Silver DJ, et al. New advances and challenges of targeting cancer stem cells. Cancer Res 2017;77:5222–7.
34. Vassilopoulos A, Chisholm C, Lahusen T, Zheng H, Deng CX. A critical role of CD29 and CD49f in mediating metastasis for cancer-initiating cells isolated from a Brca1-associated mouse model of breast cancer. Oncogene 2014;33:5477–82.

Downloaded from http://aacrjournals.org/cancerdiscovery/article-pdf/9/1/96/1847835/96.pdf by guest on 27 August 2022

35. Sanjana NE, Shalem O, Zhang F. Improved vectors and genome-wide libraries for CRISPR screening. Nat Methods 2014;11:783–4.
36. Ponta H, Sherman L, Herrlich PA. CD44: from adhesion molecules to signalling regulators. Nat Rev Mol Cell Biol 2003;4:33–45.
37. Toole BP. Hyaluronan: from extracellular glue to pericellular cue. Nat Rev 2004;4:528–39.
38. Slomiany MG, Dai L, Tolliver LB, Grass GD, Zeng Y, Toole BP. Inhibition of functional hyaluronan-CD44 interactions in CD133-positive primary human ovarian carcinoma cells by small hyaluronan oligosaccharides. Clin Cancer Res 2009;15:7593–601.
39. Kolev VN, Tam WF, Wright QG, McDermott SP, Vidal CM, Shapiro IM, et al. Inhibition of FAK kinase activity preferentially targets cancer stem cells. Oncotarget 2017;8:51733–47.
40. Golubovskaya VM. FAK and Nanog cross talk with p53 in cancer stem cells. Anticancer Agents Med Chem 2013;13:576–80.
41. Mizuno H, Kitada K, Nakai K, Sarai A. PrognoScan: a new database for meta-analysis of the prognostic value of genes. BMC Med Genomics 2009;2:18.
42. van der Toom EE, Verdone JE, Gorin MA, Pienta KJ. Technical challenges in the isolation and analysis of circulating tumor cells. Oncotarget 2016;7:62754–66.
43. Yu M, Stott S, Toner M, Maheswaran S, Haber DA. Circulating tumor cells: approaches to isolation and characterization. J Cell Biol 2011;192:373–82.
44. Warkiani ME, Khoo BL, Wu L, Tay AK, Bhagat AA, Han J, et al. Ultra-fast, label-free isolation of circulating tumor cells from blood using spiral microfluidics. Nat Protoc 2016;11:134–48.
45. Karabacak NM, Spuhler PS, Fachin F, Lim EJ, Pai V, Ozkumur E, et al. Microfluidic, marker-free isolation of circulating tumor cells from blood samples. Nat Protoc 2014;9:694–710.
46. Maddipati R, Stanger BZ. Pancreatic cancer metastases harbor evidence of polyclonality. Cancer Discov 2015;5:1086–97.
47. Salhia B, Trippel M, Pfaltz K, Cihoric N, Grogg A, Ladrach C, et al. High tumor budding stratifies breast cancer with metastatic properties. Breast Cancer Res Treat 2015;150:363–71.
48. Au SH, Storey BD, Moore JC, Tang Q, Chen YL, Javaid S, et al. Clusters of circulating tumor cells traverse capillary-sized vessels. Proc Natl Acad Sci U S A 2016;113:4947–52.
49. Perrais M, Chen X, Perez-Moreno M, Gumbiner BM. E-cadherin homophilic ligation inhibits cell growth and epidermal growth factor receptor signaling independently of other cell interactions. Mol Biol Cell 2007;18:2013–25.
50. Muller WA, Weigl SA, Deng X, Phillips DM. PECAM-1 is required for transendothelial migration of leukocytes. J Exp Med 1993;178:449–60.
51. Peach RJ, Hollenbaugh D, Stamenkovic I, Aruffo A. Identification of hyaluronic acid binding sites in the extracellular domain of CD44. J Cell Biol 1993;122:257–64.
52. Marlin JW, Chang YW, Ober M, Handy A, Xu W, Jakobi R. Functional PAK-2 knockout and replacement with a caspase cleavage-deficient mutant in mice reveals differential requirements of full-length PAK-2 and caspase-activated PAK-2p34. Mamm Genome 2011;22:306–17.
53. Reddy PN, Radu M, Xu K, Wood J, Harris CE, Chernoff J, et al. p21-activated kinase 2 regulates HSPC cytoskeleton, migration, and homing via CDC42 activation and interaction with beta-Pix. Blood 2016;127:1967–75.
54. Rudel T, Bokoch GM. Membrane and morphological changes in apoptotic cells regulated by caspase-mediated activation of PAK2. Science 1997;276:1571–4.
55. Zhang Y, Wester L, He J, Geiger T, Moerkens M, Siddappa R, et al. IGF1R signaling drives antiestrogen resistance through PAK2/PIX activation in luminal breast cancer. Oncogene 2018;37:1869–84.
56. Sarioglu AF, Aceto N, Kojic N, Donaldson MC, Zeinali M, Hamza B, et al. A microfluidic device for label-free, physical capture of circulating tumor cell clusters. Nat Methods 2015;12:685–91.
57. Labelle M, Begum S, Hynes RO. Direct signaling between platelets and cancer cells induces an epithelial–mesenchymal-like transition and promotes metastasis. Cancer Cell 2011;20:576–90.
58. Yang J, Yan R, Roy A, Xu D, Poisson J, Zhang Y. The I-TASSER Suite: protein structure and function prediction. Nat Methods 2015;12:7–8.
59. Kozakov D, Hall DR, Xia B, Porter KA, Padhorny D, Yueh C, et al. The ClusPro web server for protein–protein docking. Nat Protoc 2017;12:255–78.
60. Chen H, Sun Y, Shen Y. Predicting protein conformational changes for unbound and homology docking: learning from intrinsic and induced flexibility. Proteins 2017;85:544–56.
61. Oliwa T, Shen Y. cNMA: a framework of encounter complex-based normal mode analysis to model conformational changes in protein interactions. Bioinformatics 2015;31:i151–60.
62. Alexander N, Woetzel N, Meiler J. bcl::Cluster: A method for clustering biological molecules coupled with visualization in the Pymol Molecular Graphics System. IEEE Int Conf Comput Adv Bio Med Sci 2011;2011:13–8.
63. Brown W. Some experimental results in the correlation of mental abilities. Br J Psychol 1910;3:296–322.
64. Spearman CC. Correlation calculated from faulty data. Br J Psychol 1910;3:271–95.

Downloaded from http://aacrjournals.org/cancerdiscovery/article-pdf/9/1/96/1847835/96.pdf by guest on 27 August 2022